The Detection of Seismicity on Icy Ocean Worlds by Single-Station and Small-Aperture Seismometer Arrays

A. G. Marusiak[1†], N. C. Schmerr[1], E. C. Pettit[3], B. Avenson[3], S. H. Bailey[3]4 V. J. Bray[4], P. Dahl[5], D. N. DellaGiustina[4], N. Wagner[4,6], R. C. Weber[7]

[1]University of Maryland, Geology Department, 8000 Regents Drive, College Park, MD 20742.

[2]Oregon State University, College of Earth, Ocean, and Atmospheric Sciences, 104 CEOAS Admin Building, Corvallis OR 97331

[3]Silicon Audio, 1019 S Heatherwilde Blvd Suite 200, Pflugerville, TX, USA 78660

[4]University of Arizona Lunar and Planetary Laboratory, 1629 E University Blvd, Tucson, AZ, USA 8572551-0092

[5]Applied Physics Laboratory, University of Washington, 1013 NE 40th St., Seattle, WA, USA 98104

[6]University of Alaska Fairbanks, Department of Geosciences, 900 Yukon Drive, Fairbanks, AK, USA 99775

[7]NASA Marshall Space Flight Center, 320 Sparkman Drive, Huntsville, AL USA 358305

Corresponding author: Angela G Marusiak (marusiak@jpl.nasa.gov, angela.marusiak@gmail.com)

†Current Address: Jet Propulsion Laboratory, California Institute of Technology, 4800 Oak Grove Drive, M/S 183-601, Pasadena, CA 91109, USA

Key Points:

- Small-aperture arrays (2m) have higher detection rates (9-46%) of regional and teleseismic events compared to a single-station
- Low noise sites have a higher detection rate of global tectonic events
- A single-station seismometer in an icy ocean world analog setting can effectively detect and locate local seismicity

Abstract

Future mission carrying seismometer payloads to icy ocean worlds will measure global and local seismicity to determine where the ice shell is seismically active. We use two locations, a seismically active site on Gulkana Glacier, Alaska, and a more seismically quiet site on the northwestern Greenland Ice Sheet as geophysical analogs. We compare the performance of a single-station seismometer against a small-aperture seismic array to detect both high (> 1 Hz)

and low (< 0.1 Hz) frequency events at each site. We created catalogs of high frequency (HF) and low frequency (LF) seismicity at each location using the automated Short-Term Average/ Long-Term Average technique. We find that with a 2-meter small-aperture seismic array, our detection rate increased (9 % for Alaska, 46% for Greenland) over the single-station approach. At Gulkana, we recorded an order of magnitude greater HF events than the Greenland site. We ascribe the HF events sources to a combination of icequakes, rockfalls, and ice-water interactions, while very high frequency events are determined to result from bamboo poles that were used to secure gear. We further find that local environmental noise reduces the ability to detect low-frequency global tectonic events. Based upon this study, we recommend that future missions consider the value of the expanded capability of a small array compared to a single station, design detection algorithms that can accommodate variable environmental noise, and assess the potential landings sites for sources of local environmental noise that may limit detection of global events.

Plain Language Summary

To better prepare for future planetary missions, we deployed seismometers on glaciers and ice sheets, environments on Earth that mimic those of icy ocean worlds. We compare the ability of a single seismometer versus several seismometers in detecting different types of earth and ice quakes and to compare widely different sites with respect to local environmental noise such as ice cracking, melt water from the glacier, and rock falls off nearby mountains. We find that multiple instruments separated by only 1 m can better detect large tectonic events than only one instrument. Further, if the site has low level of environment noise, we detect more large tectonic events. Small local events, however, can help characterize the local environment. We also detected events from equipment left at our field site. Future missions would benefit from sending multiple seismometers instead of just one. If a mission wants to study the whole planet

or moon, then the landing site should be situated away from any active surface features and a single seismometer should be sufficient. If the goal is to study a specific active feature or region, then the landing site needs to be close to that feature.

1 Introduction

Icy ocean worlds are bodies in the outer solar with thick ice shells overlying liquid subsurface oceans. Notable icy ocean worlds include Europa, Ganymede, and Callisto in the Jovian system, Enceladus and Titan in the Saturnian system, and the Pluto-Charon system. Icy ocean worlds come in a wide range of sizes, from Enceladus which is only ~250 km in radius (Iess et al., 2010; Nimmo & Pappalardo, 2016), up to Titan, one of the largest moons in the solar system with a radius of ~ 2900 km and methane rich atmosphere (Smith, 1980; West et al., 1983). The internal structures of the icy ocean worlds show a high degree of variability. Callisto and Ganymede have very thick ice crusts (>100 km) (Schubert et al., 2004), while Europa or Enceladus may have ice shells that are only several to tens of kilometers thick (Billings & Kattenhorn, 2005; Iess et al., 2014; Nimmo et al., 2003; Schubert et al., 2007, 2009). Observations from spacecraft missions have provided ample evidence for subsurface oceans existing today. The Cassini spacecraft observation of active plumes implies a regional-scale sea or ocean exists at the South Pole of Enceladus. The crisscrossing faults at the surface of Europa observed by the Galileo mission have also been used to argue for the presence of liquid water beneath the surface (M. H. Carr et al., 1998). One of the strongest pieces of evidence for subsurface oceans comes from magnetometer measurements of the expected induced field that would come from a liquid water ocean. These induced magnetic fields were measured by the Galileo magnetometer instrument and validate that liquid water is present beneath the icy crust (Khurana et al., 1998). Galileo made similar observations for Jupiter's moon Callisto (Zimmer et

al., 2000). Additional geologic evidence such as crater morphologies, gravity data, topographic estimations, and cryovolcanic features also provide supporting evidence for global oceans on Europa (Pappalardo et al., 1999).

A lack of craters at the surfaces of Europa, Enceladus, and Titan suggests their ice shells are geologically young (< 60 Mya) and experience resurfacing (Bierhaus et al., 2009; Zahnle et al., 2003). For example, the Galileo mission imaged extensive faults on Europa's surface, uncut by craters (Greeley et al., 2000). There is evidence that the surfaces are active in the modern era, as during Cassini flybys, plumes were seen erupting from Enceladus's southern pole (Porco et al., 2006), and telescopic observations have suggested there may be active plumes on Europa (Roth et al., 2014). Both the faults and plumes were linked to tidal interactions between the moons and their host planets (Greeley et al., 2004; Greenberg et al., 2003; Rhoden et al., 2015; Sotin et al., 2009; Wahr et al., 2009). Tidal interactions in the form of diurnal cycles (Hoppa et al., 1999; Hurford et al., 2009) and non-synchronous rotation (Rhoden et al., 2012; Wahr et al., 2009) create stresses and tidal heating in the ice shells (Carr et al., 1998; Meyer & Wisdom, 2007; Roberts & Nimmo, 2008; Sotin et al., 2002, 2009; Tyler, 2008). These stresses manifest as strike-slip faulting (Prockter et al., 2000; Tufts et al., 1999) and normal faulting (Nimmo & Schenk, 2006) observed on the surface. Some studies postulate that subsumption and convection may be possible within the ice shells (Bland & McKinnon, 2017; Kattenhorn & Prockter, 2014; Showman & Han, 2005), others dispute this idea (Johnson et al., 2017). In addition to fracturing the surface of icy ocean worlds, tidal forces and heating can also support subsurface liquid water oceans (Matsuyama et al., 2018). A seismometer deployed on a lander is the ideal instrument, in order to provide further information about the ice structure and dynamics on these icy satellites.

Here we show results from an Earth analog study designed to help with decision making with respect to instrumentation, site selection, and on-board analysis for a future mission.

2 Motivation for Seismic Study of Icy Ocean Worlds

Icy ocean worlds have been listed as a top priority in multiple NASA Decadal Surveys (National Research Council, 2003; The National Academy of the Sciences, 2011), the Outer Planet Assessment Group Roadmap (OPAG, Hendrix et al., 2018), and the icy ocean world community (Marusiak, Vance, et al., 2021; Vance, Behounkova, et al., 2021; Vance, DellaGiustina, et al., 2021). A primary reason for this priority is their potential of habitability. Beneath their thick ice shells, lie subsurface oceans that could harbor environments suitable for biologic activity (Hand et al., 2009; Parkinson et al., 2008; Raulin, 2008; Reynolds et al., 1983). Tidal heating could help support long-lived oceans. The composition of observed plumes (Bouquet et al., 2015; Parkinson et al., 2008; Waite et al., 2017) and possible subsurface material on Europa's surface (McCord et al., 1999; Sohl et al., 2002, 2010) further suggested habitable conditions exist in the subsurface oceans. Cassini observed molecular hydrogen in the plumes from the South Pole of Enceladus which may indicate hydrothermal activity at the ocean-rock interface. On Earth, diverse lifeforms thrive at hydrothermal vents. Titan's observed atmospheric and surface composition from the Huygens's probe also suggested life could inhabit the subsurface (Raulin, 2008).

A fundamental reason icy ocean worlds are of interest is that they may be amongst the most seismically active bodies in the solar system (Hurford et al., 2020; Vance, Kedar, et al., 2018). A future mission to an icy ocean world can investigate the seismicity of that body to better understand the response to tidal stresses and internally generated stresses. For example, events deep within the ice shell may indicate that subsumption is occurring (Bland & McKinnon, 2017; Kattenhorn

& Prockter, 2014; Katterhorn & Hurford, 2009). Seismicity will indicate if and where strike-slip or extensional faulting is actively occurring, and whether it agrees with current models of stress in ice shells (Hurford et al., 2020; Nimmo & Gaidos, 2002; Rhoden et al., 2012). Observed faults on Europa are modeled to be capable of producing events with magnitudes above Mw 5.5 (Nimmo & Schenk, 2006; Panning et al., 2006; Vance, Kedar, et al., 2018). A large teleseismic event will create multiple surface wave orbits that can be used to determine the distance to the event, even if the seismic velocity structure of the planet is not yet fully constrained (Bose et al., 2017; Khan et al., 2016; Panning et al., 2015). The observation of body waves phases will help to constrain internal layering such as ice-ocean, ocean-mantle, and other internal boundaries. Focal mechanisms and source parameters of the large events will reveal seismically active regions and the underlying stresses present on faults (Fan & Wallace, 1991; Jiménez et al., 1989; Kim et al., 2000). The waveforms from seismic events can be used to determine the thickness of the ice shell, detect pockets of liquid water within the ice shell, and determine the depth of the subsurface ocean (Lee et al., 2003).

In addition to rarer, large events, icy ocean worlds are predicted to experience numerous smaller magnitude seismic events. Ice cracking and other tectonic perturbations (here referred to as icequakes) are likely to occur throughout the tidal cycle (Hurford et al., 2020). These types of events will provide information on the local crustal structure, including any subsurface liquid deposits, and the presence of porosity and water table depth. Another possibility is the detection of seismicity originating from cryovolcanic activity and liquid transport through the ice shell (Lopes et al., 2013; Porco et al., 2006; Quick et al., 2013). As liquid moves within the ice shell and erupts onto the surface, we would expect to see seismic signals similar to those of terrestrial volcanism and magmatism (Chouet, 1996; Kieffer, 1984; McNutt & Roman, 2015). Additional

seismic signals from ice-water interactions could produce seismic signals similar to those observed in cryosphere settings (Podolskiy & Walter, 2016). The chaos terrains on Europa are suggested to have formed from subsurface liquid water approaching the surface (Greenberg et al., 1999; O'Brien et al., 2002; Schmidt et al., 2011). These reservoirs of liquid water produce geophysical contrasts that are similar to those found at subglacial lakes found in Antarctica and Greenland (Bowling et al., 2019; Isanina et al., 2009; Palmer et al., 2013; Peters et al., 2008). Like terrestrial investigations, seismic deployments on icy ocean worlds could reveal the presence and size and state of the subsurface liquid water pockets. Seismic signals originating near the liquid water may also indicate if and how the water remains stable and is exchanged within the ice shells.

The terrestrial cryosphere and hydrosphere are host to a wide variety of seismicity that can serve as an environmental analog for studying icy ocean world seismicity. Glaciers and ice-sheets have signature cryoseismic signals from basal motion, icequakes, and calving events (Podolskiy & Walter, 2016). Seismometers have been deployed to Arctic and Antarctic regions to monitor ice sheets, ice loss from climate change, and water-ice interactions (Amundson et al., 2012; Clinton et al., 2014; Mordret et al., 2016; Winberry et al., 2009). In addition to unique seismic sources, the cryosphere produces unique types of seismic waves. Crary and flexural waves were identified where ice overlies liquid water and have been investigated to determine ice sheet thickness (Crary, 1955; Ewing et al., 1934; MacAyeal et al., 2015). Seismometers on icy ocean worlds would likewise be used to monitor conditions of the ice shell and detect ice-water interactions within the ice shells. On Earth, the oceans are responsible for microseismic noise that can be detected anywhere on Earth (Ardhuin et al., 2001). Correspondingly, seismometers could monitor hydrocarbon lakes on Titan (Stähler et al., 2019).

Seismic events, and events that are tied to the unique seismic environments found across the planets, can help characterize the local environment and reveal the inner workings of planetary environments. For example, the Apollo seismic experiments revealed deep moonquakes, near-surface thermal events, contractional tectonic events, as well as meteorite impacts. The deep moonquakes, which are the most common type of lunar event, were caused by tidal interactions with the Earth and Sun (Bulow et al., 2007; Kawamura et al., 2017). The shallow moonquakes are inferred to be contractional tectonic events that imply the Moon is shrinking as it cools (Watters et al., 2019). Thermal moonquakes have been temporally linked to sunrise and sunset and diurnal temperature cycles (Duennebier & Sutton, 1974). Likewise, the InSight mission to Mars is building its catalog of events which fall into several categories. Early results indicate that Martian seismicity falls between the Earth and the Moon (Giardini et al., 2020). The Martian events tended to excite different frequency ranges, which may point to differences in their sources. Joint investigations between InSight's Seismic Experiment for Interior Structure (SEIS) instrumentation and meteorological instruments have investigated atmospheric phenomena such as daily changes in wind speed and direction, and dust devils (Banfield et al., 2020; Perrin et al., 2020). Larger events (in terms of magnitude) have been used to recover the crustal thickness (Knapmeyer-Endrun et al., 2021), mantle structure (Khan et al., 2021), and the size and state of the core (Stähler et al., 2021). Missions to icy ocean worlds would like-wise benefit from seismic deployments and bring new insights to the seismicity of these worlds.

At present, there are concept missions, the Europa Lander (Hand et al., 2017) and an Enceladus Orbilander (Mackenzie et al., 2021), as well as the selected New Frontiers mission to Titan, Dragonfly (Barnes et al., 2021; Lorenz et al., 2019), that would carry seismic payloads. The mission science goals include constraining internal structure and investigating seismicity. There

194 are many associated challenges in predicting the seismicity that these missions will observe. Titan
195 has a thick atmosphere and lakes which could contribute to environmental noise and potentially
196 activate spacecraft resonances (Stähler et al., 2017; Vance, Panning, et al., 2018). Europa has a
197 high level of radiation at its surface (Paranicas et al., 2007), thus the expected lifetime of a lander
198 mission is limited to a few weeks of seismic recording (Hand et al., 2017). Due to the short time
199 frame of a Europa mission, data would likely be sent using a low sampling rate, and if a detection
200 is made, higher sampling rates could be later sent back to Earth. It has been proposed that the
201 mission have only a single-station seismometer or be confined within a small-aperture array (< 2
202 m). This means there will be a location bias associated with detected events. For example, the
203 Apollo experiments were only able to detect deep moonquakes on the near-side of the Moon. It is
204 still uncertain whether a lack of far-side detections was due to the absence of events, or if the
205 properties of the lunar interior inhibited their detection. Likewise for InSight, a blind test was able
206 to show that the detection of an event is related to the size of the event and the distance from the
207 source (van Driel et al., 2019) such that only larger events can be detected at greater distances.

208 The ability to detect both large teleseismic and smaller, local events will be critical for the
209 success of future seismology-driven missions. Due to data and/or cost restrictions, a single-station
210 may be preferred over a small array of stations. However, the array would provide additional data,
211 enhanced signal-to-noise, as well as necessary redundancy in the event of instrument failure. Here,
212 we test how single-stations and the small-aperture arrays could detect tectonic events through
213 automated detection. We further study how these automated algorithms perform against operator
214 inspection of the dataset for events. This allows for quantification of the advantages of a small-
215 aperture array over a single-station and assess whether there is justification for improving the
216 automated detection algorithms. Here, the small-aperture array is limited to a few square meters,

mimicking the deployment of instruments on a lander, which is limited to the use of a robotic arm or deployment on spacecraft landing gear. We note that in previous deployments of small-aperture arrays on the Moon that stations were separated by several hundreds of meters (Kovach & Watkins, 1973) and terrestrial small-aperture arrays are typically kilometers in scale (Manchee & Weichert, 1968).

Given the limited bandwidth for transmission of data, we also study how well automated detection algorithms work under two separate seismicity regimes for isolating impulsive (short duration) events from either natural environmental noise or equipment-induced noise. In practice, local environmental noise signals may be of high value to scientists, whereas equipment-induced noise may not. For simplicity, we refer to both types of noise in this manuscript as "environmental noise". We study how detection rates varies between a tectonically and seismically more active site to a low noise site farther from an active plate boundary and predicted sources of local seismicity (e.g. rockfalls, calving events). To detect events, we employ the short-term average/long-term average (STA/LTA) approach after applying bandpass filters. For the small-aperture array, the same approach applies, but to be counted as a plausible detection, an event needs to trigger the detector for the majority of the stations; in other words, the detection threshold has to be met by more than one (or two) station(s). We ground-truth our results against known event catalogs (U.S. Geological Survey, 2020) to determine how many events are detected, how many are missed, and how many events we could potentially add to the catalog. We also use operator inspected seismograms and spectrograms to search for events that were not included in the automated catalog to understand how and why the automated detection algorithm failed. For high frequency events, we perform a cluster analysis to distinguish between potential sources. The cluster analysis categorizes events by waveform and then recovers location and timing

information. If clusters share characteristics, this can help locate them and identify potential sources. For icy ocean worlds, this type of cluster analysis will be useful to investigate where and when events in the ice shell occur. For example, cluster analysis may provide insight into rift zones on Europa, the tiger stripe features on Enceladus, or how seismicity changes with the tidal cycle.

3 Icy Ocean World Geophysical Analog Site and Data Collection

To compare a single-station seismometer to a small-aperture array of seismometers, we deployed seismometers at two separate terrestrial sites selected to have geophysical characteristics that produce seismic signals similar to what we would expect to occur at an icy ocean world. Both investigations are part of the Seismometer to Investigate Ice and Ocean Structure (SIIOS) project. We selected sites with thick ice (> 100 m) overlying some degree of liquid water, in proximity to the abundant seismicity of an active subduction zone, or a region of low tectonic activity (stable cratonic regions). Our selected sites were Gulkana Glacier in the Alaska Range (Marusiak et al., 2020) and a site in northwest Greenland (Figure 1) (Marusiak, Schmerr, et al., 2021).

Gulkana Glacier represents the high environmental noise, potentially active, site on an icy ocean world. Gulkana Glacier is located in the Alaska Range near Ogive Mountain and Skull Peak. Gulkana Glacier was also selected for logistical and accessibility reasons and due to its status as a benchmark glacier that has been extensively characterized (Baker et al., 2018; Van Beusekom et al., 2010). Ice thickness beneath the seismic deployment is ~100 m (March, 2000; Ostenso et al., 1965) and as the site is in the ablation area, the presence of firn or snow on top of the glacial ice was patchy and never more than 50 cm. The local topography in the peaks surrounding the site ranges from ~1200 m to ~2000 m (March & Trabant, 1997; Ostenso et al., 1965). Gulkana Glacier is situated near the Alaska-Aleutian subduction zone (Argus et al., 2011) (<20° epicentral distance) and there is typically abundant regional seismicity that includes large (Mw > 4) earthquakes.

During the Gulkana Glacier deployment, the largest teleseismic event we recorded was a Mw 7.1 that occurred in Mexico on 19 September 2017, and there were four events with $M_w > 6.0$. Steep moraine slopes with loose rock in the vicinity of the array produced a number of rockfall events,

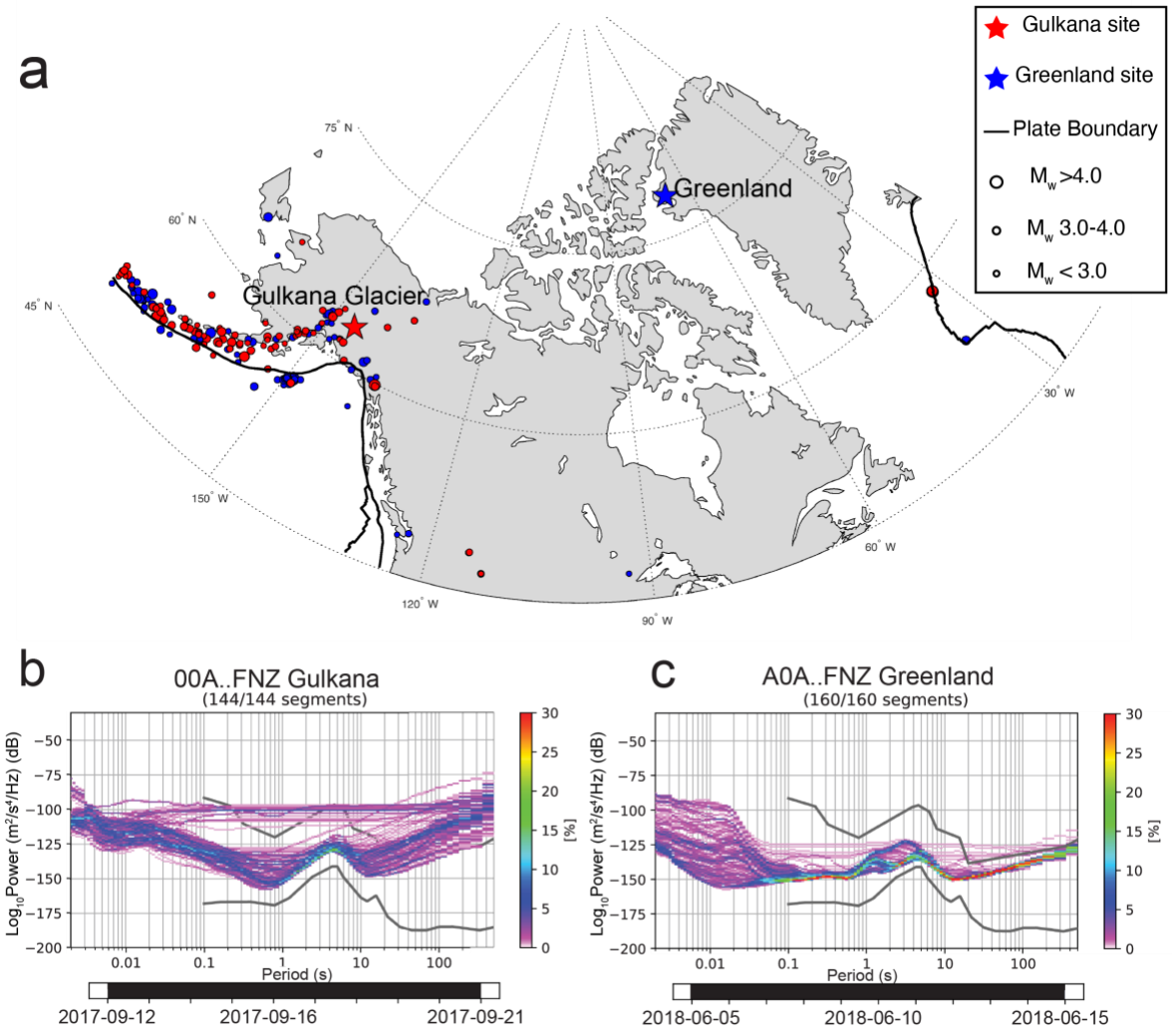

Figure 1. a) Map of SIIOS experiment locations on Gulkana Glacier (red star) and in Greenland (blue star). Gulkana is situated in the vicinity of the Aleutian-Alaskan subduction zone and Pacific-North American plate boundary. Earthquakes (circles) are color coded by whether they occurred during the Greenland (blue) or Gulkana (red) passively recording deployment dates, and with symbol size corresponding to event magnitude. Plate boundaries (black lines) are from Argus et al., 2011. b) Power density spectrum probability density function for 1-hour long segments for station 00A at Gulkana Glacier showing the local noise at the station. c) Power density spectrum probability density function for the Greenland station A0A for background noise. In parts b) and c) the bar at the bottom indicates the time window for the station noise sample for the PDS-PDF. Values for the PDS-PDF were calculated using the McNamara and Buland (2004) method. The gray lines are NHNM and NLNM from Peterson, 1993.

with many rockfall events audible during installation, especially near sunset and sunrise. Average daily temperatures at the site during the deployment ranged from -3 to 10 ºC (US Geological Survey, 2020), with substantial melt occurring during the day, evidenced by several active moulins within 30-50 meters of the array. During the daytime, we observed abundant surface runoff organized into small stream systems on the surface of the glacier, as well as larger stream drainage at the terminus of the glacier.

Our experiment site on the Greenland ice sheet was chosen to be seismically quiet compared to the Gulkana Glacier experiment. The Greenland site is situated > 1000 km away from any active plate boundaries, with the nearest boundaries being the Gakkel and mid-Atlantic ridges (Argus et al., 2011). The Greenland location was also colder (-14 to -2 ºC) than the Alaska site reducing surface activity, producing quieter power density function (Figure 1c). The northwest Greenland stations were situated on ice with an underlying thickness of ~850 m (Maguire et al., 2021), of this thickness, the top 45 m is firn. The site is situated over a subglacial lake first identified by Palmer et al., 2013, and further characterized by Maguire et al., 2021, who estimate the depth of the lake at 10-15 meters. This site falls within the Mesoproterozoic Thule basin terrane and Inglefield mobile belt of northwestern Greenland (Dawes, 2009). Only 14 events above M_w 5.0 occurred during the deployment, with no events larger than a M_w 5.9. Due to the northwest Greenland location near the ice divide, the ice surface speed is < 10 m a year and there are no surface streams or moulins. We recorded data at both field sites for approximately two weeks, similar to the length of a Europa seismic deployment.

Small-aperture arrays deployed at each site consisted of one Silicon Audio in the center, with four additional Silicon Audio sensors ~1 m away in each cardinal direction. Each station recorded with a sampling rate of 1000 Hz on three orthogonal components (FNZ, FH1, FH2). For

our analysis, the instrument responses are removed, and a range of bandpass filters are applied (see Section 4 for details). We note that sensors in the Gulkana array became tilted and/or rotated over the course of the experiment owing to meltwater saturating the sand in which the instruments were buried (Marusiak et al., 2020) which affected azimuthal recovery uncertainties and data quality. Most of the Gulkana sensors still had power and were actively recording upon demobilization. The northwest Greenland sensors operated for two weeks, but burial by a summer snowstorm caused event power loss, with some stations losing power sooner than others by up to several days (Marusiak, Schmerr, et al., 2021). However, none of the northwest Greenland instruments underwent tilt or rotation from their initial recorded positions. For consistency across the field sites, we assign the single-station result to the buried station at the center of the array (Marusiak et al., 2020; Marusiak, Schmerr, et al., 2021). At both locations, the center station sensors experienced the least amount of tilt and some of the longest uninterrupted recording times. For details regarding the power density functions, tilt directions, rotations, and exact geometries at the Gulkana Glacier site see Marusiak et al., (2020) and the northwest Greenland site, (Marusiak, Schmerr, et al., 2021).

4 Methods

We explore a suite of methods to compare detection capabilities for the expected range of seismic sources present in our field sites. We use these tools to detect the seismic sources, and where possible, characterize azimuths using a suite of automated and interactive seismic operator techniques. To detect low-frequency (LF) regional and teleseismic, and high frequency (HF) local events we use the vertical component of seismic data in a STA/LTA approach (Baer & Kradolfer, 1987; Withers et al., 1998), and when attempting to detect nearly identical very-high frequency signals, we implement a template detector which takes advantage of cross-correlation between

waveforms to make detections (Forghani-Arani et al., 2013). The template approach is only used for events that produce source time functions that were highly auto-correlated to one-another. The template for the cross-correlation approach uses a short period (~0.5 seconds) of selected signals that represents desired characteristics in a relatively low noise environment. We use built-in functions of the Python ObsPy module, namely the correlation detector for the template detections, the classic STA/LTA for single-station approaches, and the coincidence trigger for the small-aperture array STA/LTA approach (Beyreuther et al., 2010). Catalogs of regional and teleseismic activity (U.S. Geological Survey, 2020) were downloaded and we search for events to determine which events are detectable using visual inspection for comparison to the auto-detector.

We targeted different algorithms for different types of events within the dataset. Teleseismic and regional events are of high interest to planetary missions as they sample globally and interact with the deeper interior of a planet. Their longer travel paths and deeper sampling leads to these events tending to have lower-frequency content (from 0.02 to 5 Hz) waveforms that occur over longer durations (several seconds to several minutes long) than local events such as icequakes (Podolskiy & Walter, 2016). As more distant events tend to have lower frequency content owing to attenuation along their path in the mantle and crust, we implement two different bandpass filters. The first searches for more distant, teleseismic events using corners of 0.02 and 1 Hz. The second searches for closer, regional events and uses corner frequencies of 0.1-5 Hz. The corner frequencies are based on previously published values (Trnkoczy, 1999; Withers et al., 1998), and trial and error to identify the frequencies best suited for the detection. During visual inspection we noted some glitches and false positives. See section 5 for more details.

High frequency (HF, 2 to 20 Hz) events represent the expected signals of icequakes, moulin activity, and/or rockfalls. These events have been observed in polar environments and provide

insight into a variety of local processes related to glacier or ice sheet flow, fracture, or melt. Thermally induced icequakes in East Antarctica, for example, have characteristic frequencies between 5-20 Hz and typically have durations of 1.5 seconds (Lombardi et al., 2019). Recently icequakes in Antarctica were identified and shown to correlate with tidal stresses suggesting similar seismic activity could be detected at the south pole of Enceladus (Olsen et al., 2021).

During visual inspection of the data, we discovered another very high frequency (VHF) signal in the northwest Greenland stations that was subsequently also detected in the Gulkana Glacier stations. These VHF signals consist of repeating wavelets at semi-regular intervals 0.1 seconds. As these events have characteristic repeating signals, we adopt a template detector in an attempt to catalog their occurrence and duration. We chose a small section containing several of the repeating signals of high quality. The template detector looks for high coherence between the template and recorded signals to find similar looking recordings.

To attempt to determine the HF and VHF event's location, we implement a polarization approach (Stachnik et al., 2012) to determine azimuth. The polarization approach examines how a seismic wave's energy is divided among the orthogonal components (vertical and two horizontals) to determine the direction from which the wave likely arrived. As it is often difficult to identify *P*, *S*, or surface waves, the entire waveform is used. For the same reason, we do not attempt to determine the distance between source and receiver since identifying multiple arriving waves is required to determine distance to an event. In the case of Gulkana, we apply a correction to back azimuths to account for rotation of the instrument during the experiment.

4.1 Automated Detections with a Short-Term Average/Long-Term Average

The STA/LTA method is used to automate the detection of *P* and *S* wave onsets and for seismic event identification (Baer & Kradolfer, 1987; Withers et al., 1998). The method uses a

short-term average amplitude of a seismogram and that is then compared to a longer-term time window average of amplitudes through division, resulting in a ratio. The value of the ratio is chosen by an operator to determine where it indicated that a short-term deviation from the running background mean is commensurate with the detection of a seismic event. To detect the LF and HF events, we use different bandpass filters on the data and set the short-term and long-term average thresholds based on experimentally determined values from literature (Trnkoczy, 1999). For distant teleseismic LF events, we use a bandpass filter of 0.02-1.0 Hz, and set the STA/LTA time window parameters to 1 and 60 seconds, respectively. A STA/LTA amplitude detection threshold is set at 20 for Gulkana Glacier, meaning the short-term average (1 second surrounding the event) has to be at least 20 times greater than the long-term average (60 seconds) to be triggered (Figure 2). In Figure 2 the onset of the *P* wave shows STA/LTA value of nearly 60, and is recorded as a detection. Owing to the overall lower environmental noise in Greenland (Figure 1), the STA/LTA threshold for the northwest Greenland site is reduced to 10. To search for LF events that were more closely situated and regional, the bandpass filter is set to 0.1-5 Hz, and the STA/LTA parameters are set at 0.5 and 30 seconds, respectively. The threshold for regional event detection is set to 35 for the Gulkana Glacier stations and 5 for the northwest Greenland stations. Greenland has lower thresholds because there were fewer events overall, and the potential recordings tend to be farther

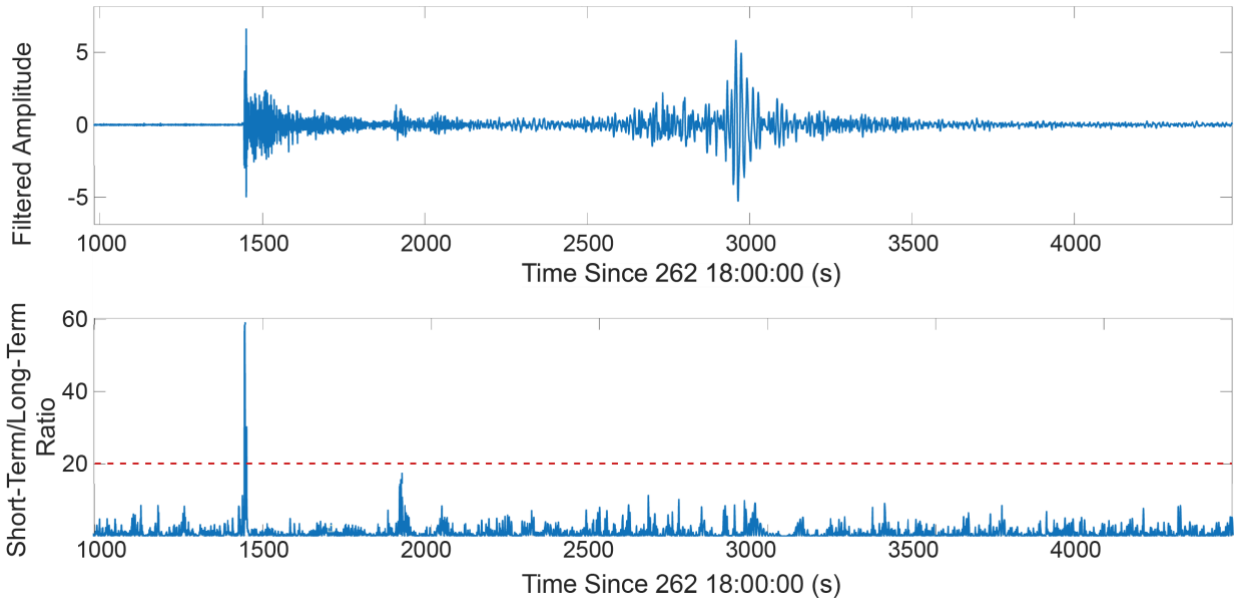

Figure 2. Example STA/LTA detection of a LF seismic event (Mexico Mw 7.1 event on 19 September 2017, 18:14:38 UTC) in our catalog. Here the time series was band-pass filtered from 0.02-1.0 Hz. The top plot shows the vertical component of motion on 00A station collected at the Gulkana Glacier array. Corresponding values of the short-term average/long-term average ratio for a 1 and 60 second window are plotted on the bottom.

distance-wise, reducing signal-to-noise ratios. By looking for known events we are able to adjust the parameters to increase detections without over-producing false positives. The reported parameters were found to produce an optimal number of true positives (events in the global catalog, detected by the STA/LTA) while reducing false negatives (clear seismic events in the data, not detected by the STA/LTA) and false positives (non-seismic events in the data, and detected by the STA/LTA). The false positives could come in the form of instrumental anomalies or glitches, discussed in more detail below. False positives could also be caused by other local signals.

Once the initial automated STA/LTA catalog detections are made, the candidate events are examined on vertical component spectrograms to determine the event duration after the event is triggered. The spectrograms are calculated using parameters based on the detection parameters. For LF events the spectrogram uses a frequency range limited to 0.01 to 50 Hz, and a time window of 50 seconds with a 25 second overlap. To remain a candidate event in our catalog, the spectrogram needs to stay above 5 dB over the mean background value for the frequencies used in

388 the respective bandpass filter for 2 seconds surrounding the start and end time of the event. The
389 duration of the event is determined by the time period that remained above 5dB over the
390 background. We also check for overlapping events by checking the end time with the next temporal
391 event in the catalog. If the subsequent event begins within 20 seconds for regional filters or 60
392 seconds for teleseismic filters, we then merge the events using the earliest onset time. Merging
393 events deals with larger teleseismic events where the *P* wave and surface waves are often separated
394 by minutes, resulting in a double detection. In our spectrogram corrected catalog, the LF-type
395 events tend to be longer in duration, lasting minutes for regional, or tens of minutes for large
396 teleseisms. To further reduce the number of false positives in the detection algorithm, events are
397 then removed from consideration if the event duration is under a minimum threshold. Minimum
398 event length is set to 10 seconds for regional events and 15 seconds for teleseismic events which
399 help to remove some instrumental anomalies.

400 The spectral analysis also help to eliminate STA/LTA false positives resulting from
401 instrumental glitches, re-centering events, or other non-seismic instrumental anomalies. Glitches
402 in the sensors are defined by sharp spike in amplitudes and increased power levels across the entire
403 frequency spectrum. Most glitches last < 10-15 seconds, further motivating our exclusion of short
404 duration detections from the candidate STA/LTA catalog. These events would pass all the previous
405 criteria, but in subsequent visual inspection are always eliminated as plausible event candidates.

406 Once the candidate events exhibit sufficient frequency content, each event is operator
407 inspected and a catalog is made that recorded the time of the event, the raw (unfiltered, but
408 instrument response removed) amplitude, filtered amplitude, dominant frequency, and event
409 duration. The events are then compared to a catalog from the USGS Advanced National Seismic
410 System (ANSS) Comprehensive Catalog (ComCat) (U.S. Geological Survey, 2020). This service

combines regional and global catalogs of earthquakes to create a more complete catalog of events than using a regional catalog. The minimum magnitude of this catalog is Mw 2.5. We use the ComCat locations, onset times, and the PREM model (Dziewonski & Anderson, 1981) in the TauP software toolkit (Crotwell et al., 1999) to calculate the predicted arrivals of surface waves (assuming a velocity of 3000 km/s) and *P* waves. If the predicted arrival times matches the start times of our catalog within ~1- 20 seconds, depending on the ComCat event distance, then the event is considered a match. There are times where an event is detected in our catalog, but no event from the ComCat catalog has a predicted arrival time that matched. We suspect that these are local events that had low magnitudes (<2.5 Mw) and were not detected by seismic stations contributing to the ANSS ComCat.

To search for potential high frequency (HF) events, we use a different set of parameters to build the catalog. HF events are detected using a bandpass filter of 5-20 Hz applied to the data (Lombardi et al., 2019). For HF events, the STA/LTA time window parameters are set to 2.5 and 40 seconds for the short- and long-term averages, respectively. The required threshold for detection is an STA/LTA value of 20 and 5 for Gulkana and Greenland, respectively. Our choices for these parameters are based on visual inspection of the filtered time-series and the values for the STA/LTA. Like the lower frequency event detections, some trial and error is involved by testing a range of values from the literature (Lombardi et al., 2019; Trnkoczy, 1999; Withers et al., 1998). As attenuation tends to remove high frequency content from events of regional or greater distances, we assume the HF events are more local (< few kilometers), and that their temporal amplitudes must fall above the high frequency environmental noise. Unlike lower frequency events, we do not inspect the spectrograms for these events. This was done for two reasons. The first is due to the higher limit of the bandpass filtered (20 Hz) which is close to where the environmental noise

may begin to dominant. It would be difficult to determine if the event is causing high values in the spectrogram, or if it is general environmental noise or glitches. The second reason was for efficiency. HF events such as icequakes are short in duration (< 2 seconds). To properly assess the event duration, one would need to calculate the spectrogram in ~0.1 s increments. For datasets consisting of ~two weeks with 1000 Hz sampling rates, the algorithm would become significantly slower. Downsampling might have addressed the efficiency issue, but it would also introduce errors from very high-frequency events. Instead of relying on spectrograms, the duration of the event relies on the STA/LTA values. The event duration is determined by the time-span that the STA/LTA minimum threshold (20 or 5) is exceeded. The minimum event duration is set to 0.25 seconds, and minimum event separation is set to 0.1 seconds, meaning events separated by less than 0.1 seconds are merged. Since the long-term average is set at 40 seconds, we could capture events up to 20 seconds long, an order or magnitude greater than their typical duration. Although spectrograms for the entire dataset are not computed, we do compute periodograms for each event in the catalog to determine the most dominant frequency of the event. The initial catalog is then visually inspected to remove events caused by VHF events or glitches. The final catalog recorded dominant frequencies from periodogram calculations, along with raw (unfiltered) amplitude, azimuth, time of event and duration of event. For these events in our catalog, azimuths are calculated using a polarization approach (Stachnik et al., 2012).

Due to the high number of HF events, we also perform a hierarchal cluster analysis. This method has previously been applied in seismic investigations of the cryosphere (Lombardi et al., 2019). The goal of the cluster analysis is to categorize events based on their waveforms and further investigate if these categories have similar back azimuths, frequency content, and/or occur at a preferred time of day which may help identify their origins. To perform the hierarchal cluster

457 analysis, we take the absolute value of the Hilbert transform of each individual waveform so we
458 can compare envelopes of energy in order to categorize events.

459 In addition to single-station approaches we also test small-aperture array approaches for
460 the lower frequency, potentially tectonic-origin events. At the Greenland field site, both a small-
461 aperture (<2 m) array and larger (< 2 km) remote array were deployed. To maintain consistency
462 between field sites, we choose to only use data from the small-aperture array for both field sites.
463 To become a candidate array event detection, 4 out of the 5 stations in the array need to have
464 STA/LTA values that exceed the threshold for candidate detection. Towards the end of the
465 northwest Greenland experiment, as stations began to lose power, we altered the candidate array
466 detection threshold to 3 out of 4, or 2 out of 3 stations, depending on how many stations were left
467 powered. To compare the single-station versus small-aperture array approaches, we use the same
468 length for the short- and long-term averages and minimum thresholds used to compute the single-
469 station STA/LTA values. Also like the single-station approach, spectrograms are generated and
470 events are visually inspected using the center single-station's vertical component.

471 4.2 Template Detection Methodology

472 A very high frequency (VHF) signal was originally observed while inspecting the
473 northwest Greenland data for potential detection failures of the high frequency events. The signal
474 can be identified by its repeating nature and characteristic spectral signature (Figure 3). The
475 repeating nature of the event allows us to create a template to perform cross-correlation detections
476 for other instances in the time series for the event. The template approach is preferred to a
477 STA/LTA as the event waveforms were very similar to one-another and have a signature repeating
478 nature. Unlike regional or teleseismic events where arrivals times of body waves and surface waves
479 vary, the waveforms of the VHF signals are nearly identical. The python code

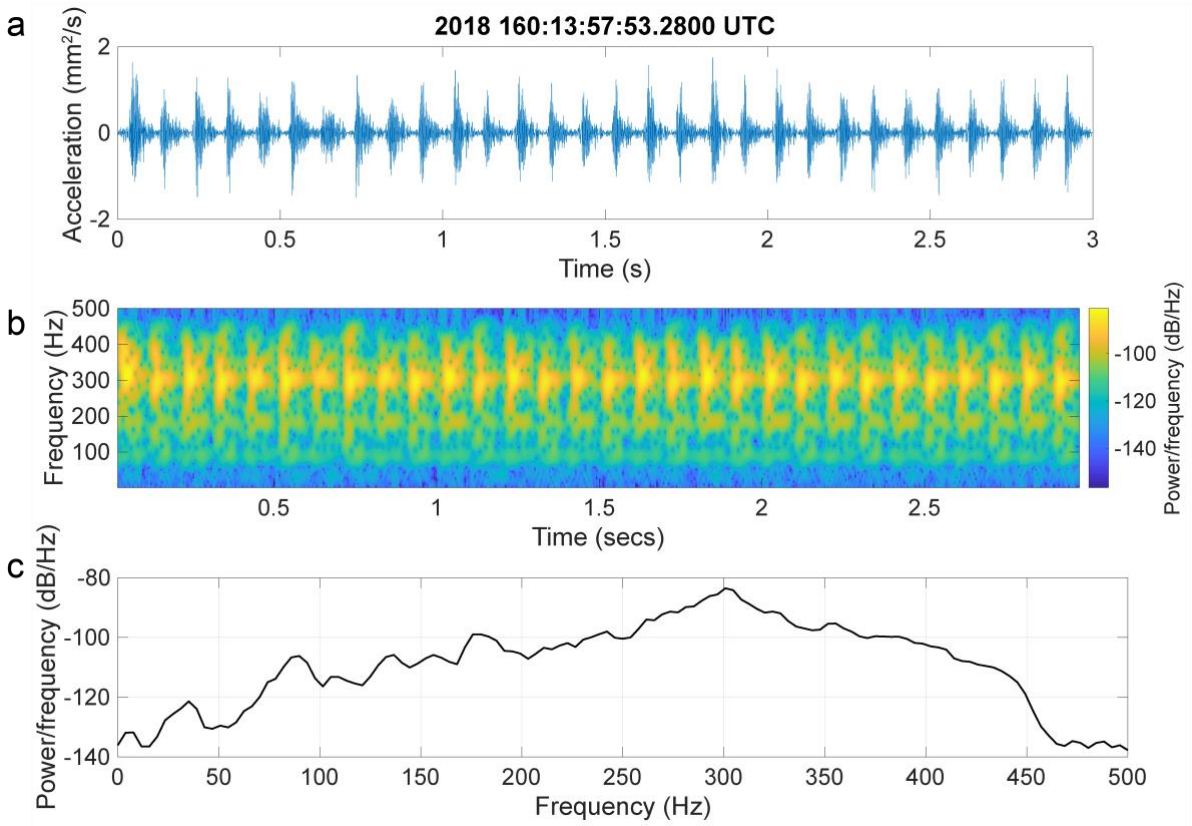

Figure 3. Example of a VHF repeating signal found in both the northwest Greenland and Gulkana Glacier datasets. Here we show an example from the Greenland, station A0A. The signals have a periodicity of ~10 Hz. a) The vertical component of motion for station A0A. b) Spectrogram computed using time windows of 0.075 second, overlapping every 0.050 seconds. c) The resulting periodogram for the same time segment. The dominant frequency is around 300 Hz with additional resonances at 175 and 90 Hz.

(*correlation_detector*) uses the template to perform a cross-correlation with the data set. The template is set as the vertical component at time 2018-06-09 13:46:52.22 and lasted for 0.6 seconds, capturing about 5 of the individual signals. A secondary template made from a stack of ten of the individual signals was also tested but tended to retrieve a large number of false positive events, meaning anything that wasn't the repeating signal. The template detector works by calculating the similarity between the dataset and the template. If the similarity exceeds a threshold of 1.0, a candidate detection was made. For each candidate template detection, we calculate the spectrogram of each event using a time window of .075 seconds overlapping 0.050 seconds. The power between 300-400 Hz must exceed 15 times the mean PSD values over all frequencies for 0.5 seconds before and after the event. The rationale for our VHF event criteria is based on the secondary algorithm for LF and HF event detection. By setting a minimum required power level over the background, false positives could be eliminated. In most cases the false-positives for VHF events are from other HF events already in our catalog that excited energy above the 20 Hz bandpass filter. We set another criterion that the maximum amplitude for a VHF event detection has to exceed 0.04 mm/s^2 on the vertical component of motion. This value is somewhat arbitrary but is determined by visually examining known signals and helps to eliminate false positive detections. If HF events occur in rapid succession, the template finder would initiate a detection, but these events tend to fail to meet the amplitude criterion. Once a VHF detection meets the template detection, periodogram, and amplitude threshold criteria, we visually inspect the event to ensure that only the desired waveforms are in the final VHF event catalog. The VHF final catalog records the time of the signal, filtered and unfiltered amplitudes, and duration.

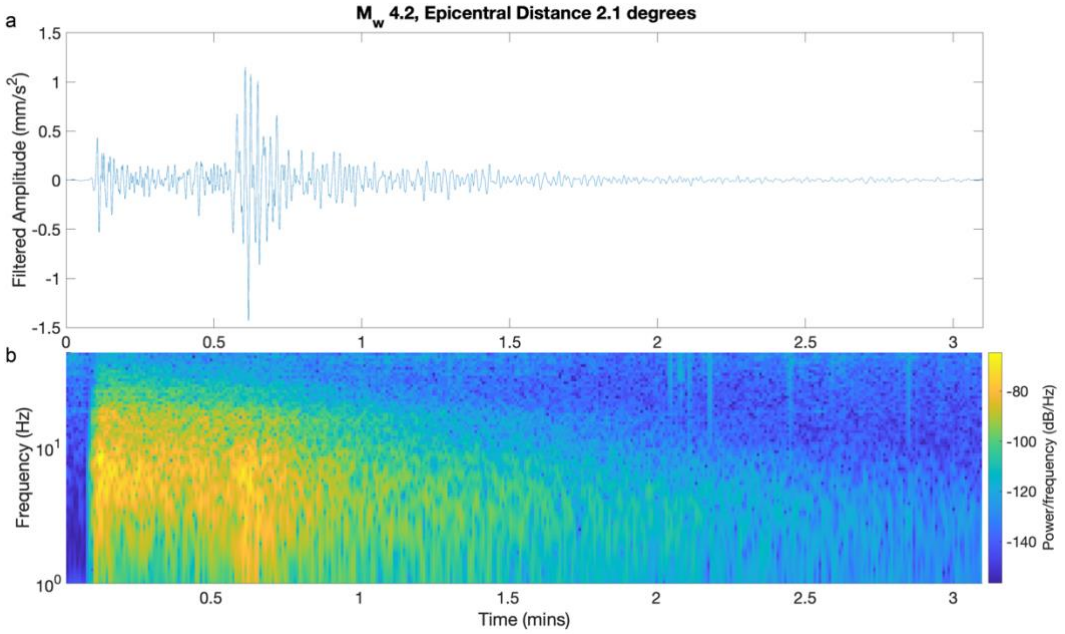

Figure 4. Example of a positive detection using the single-station approach at Gulkana Glacier. a) The vertical component time-series shows a high amplitude arrival that corresponds with the event that occurred on 13 September 2017, 07:22:17 UTC. B) Spectrogram of the data in part a). The spectral domain also shows strong power in frequencies below 10 Hz. A time window of 15 seconds, overlapping every 14.5 seconds was used to construct the spectrogram.

5 Results

5.1 Detection of LF Regional and Teleseismic Events

The single-station candidate catalog for Gulkana Glacier contains 81 LF teleseismic and 117 regional events prior to operator inspection. Out of these 198 candidate events, 130 (66%) are matched to events in the ComCat catalog. The single-station northwest Greenland candidate catalog contains 64 teleseismic and 89 regional events prior to operator inspection. Of these 153 candidate events, 85 (56%) are matched to events in the ComCat catalog. Most of the unmatched candidate events are from instrumental anomalies: 65 out 68 for Gulkana, 63 out of 68 for Greenland. Because the glitches are high amplitude in the time-series and high power (dB) across

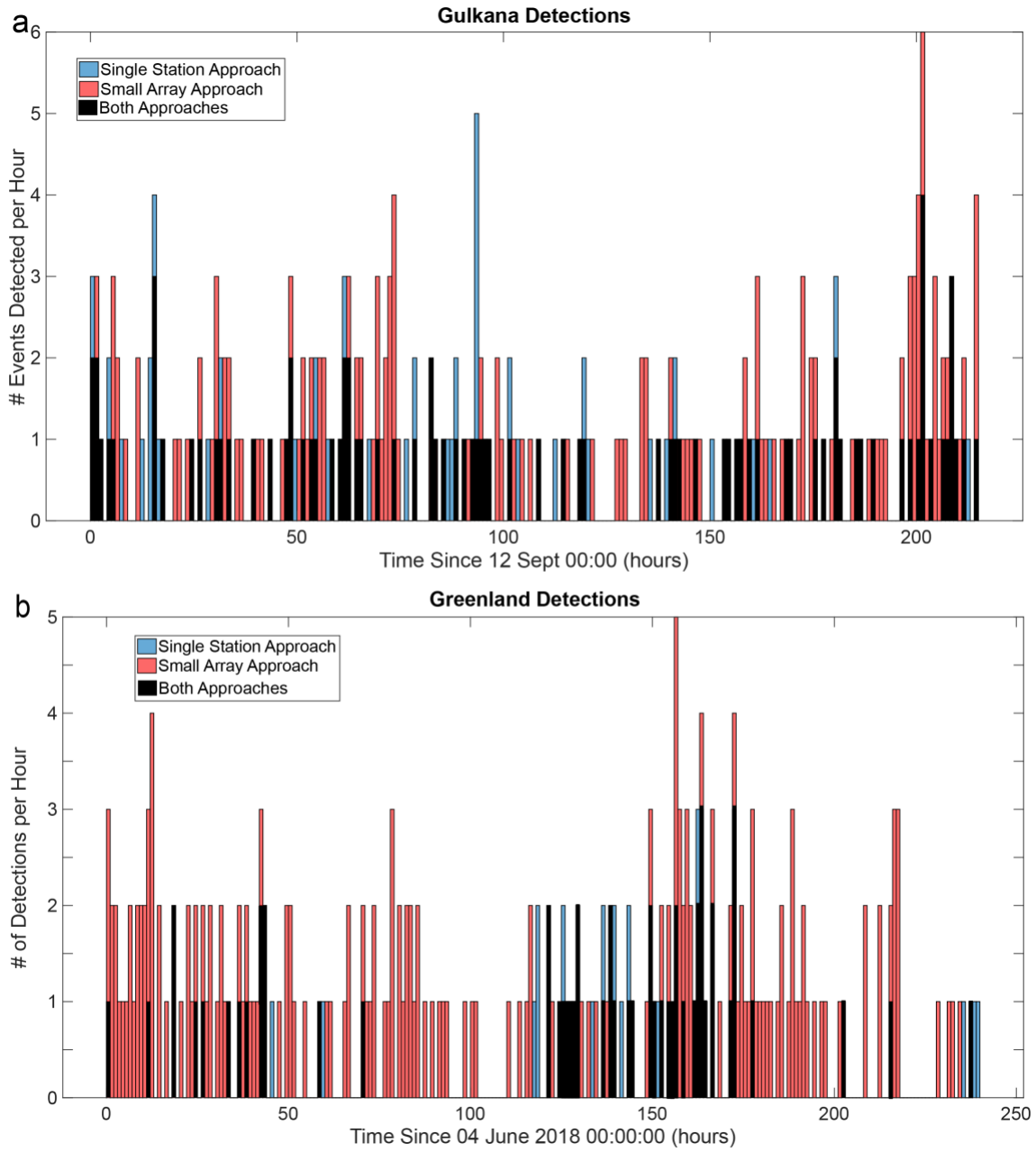

Figure 5. Final catalogs for a) Gulkana site and b) Greenland site using the single-station approach (blue), small-array approach (orange), and both approaches (black). Detection rates ranged from 0-6 detected events per hour.

all spectral ranges they have to be removed from the potential catalog by visual inspection of each event. With this straightforward STA/LTA approach, we detected only a few additional events that were not in the catalog, 3 at Gulkana Glacier and 5 events in Greenland. We are able to detect many of the large events and some of the small but nearby (<10 °) events (e.g. Figure 4). In addition

514 to the events in the ComCat catalog, there are 3 Gulkana Glacier events detected by our station
515 that are not in the catalog and 5 events detected by our station at Greenland.

516 Using the small-aperture array approach, the candidate catalog contains 135 possible
517 teleseismic events and 423 possible regional events for the Gulkana Glacier site, and 246
518 teleseismic and 188 regional events for the northwest Greenland site. Of the 558 candidate events
519 at Gulkana Glacier, 214 (38%) are attributed to an event in the ComCat. Of the 434 candidate
520 events in Greenland, 226 (52%) are attributed to events also in the ComCat. Low-Frequency event
521 detection rates at Gulkana Glacier range between about 0 and 5 per hour, for each hourlong
522 window (Figure 5a). At the Greenland site, there are one or two low-frequency events detected in
523 each hourlong window (Figure 5b). Like the single-station approach, the small-aperture array data
524 includes some events (22 for Gulkana Glacier, 7 for Greenland) that are not in the ComCat catalog.
525 The array catalog has fewer triggers from glitches, but there are still triggers from larger amplitude
526 HF events, especially for Gulkana where there are more high quality (signal-to-noise ratio) HF
527 events. We identified the HF events by their relatively short durations and higher frequency content
528 (up to 20 Hz). In total 322 (58%) events in the Gulkana Glacier candidate catalog and 201 (46%)
529 in the northwest Greenland candidate catalog are attributed to HF events or instrumental
530 anomalies.

531 We examine events with $M_w > 5.0$ or epicentral distance < 20° in the ComCat catalog but
532 were not detected by our detector (false negatives) in more detail. Of the 70 undetected ComCat
533 events for Gulkana, visual inspection shows that 18 events were recorded by our stations despite
534 not being detected by our detector. Similarly, for the Greenland site, of the possible 19 undetected
535 ComCat events, visual inspection shows that 3 events were recorded by our stations. These events
536 that are not automatically detected tend to occur either near larger, contemporaneous events or

during periods of high environmental noise. Both affected the automated detections through STA/LTA as the STA/LTA amplitude falls below the threshold for detection.

Environmental noise can have a number of sources, but one common to both of our sites that is known to cause issues in event detection is wind (Dybing et al., 2019). Figure 6 shows that our detection algorithm find fewer events when wind speed exceeds 4 m/s. Some of the events that are not detected are simply below the noise at the sites, such as a M_w 6.1 event that occurred 121° away from Gulkana Glacier, or a M_w 2.5 event that occurred 10° away from Gulkana Glacier. Both of these events happened when wind is particularly strong (~10 mph, 4 m/s) which creates a strong environmental signal. Other undetectable events tend to occur during daylight hours when nearby HF events and other local noise may obscure their arrivals. Gulkana algorithms fail to detect all 24 ComCat events that occur between 9 am and 1 pm local time. Small events tend to be obscured by larger concurrent events. Small events that occur in clusters or within short intervals are also difficult to detect visually or with the automated algorithm.

To summarize, seismologist operator review allows us to identify 75 out of 127 events (59%) for Gulkana and 26 out of 41 events (63%) for Greenland. Of the operator detected events, the final catalogs (post visual confirmation) using single-station approaches detect 38 events (51%) for Gulkana and 9 events (35%) for Greenland. Small-aperture arrays also have a higher detection rate when reviewed by a seismologist. Of the events that are operator detected, the final catalog using the small-aperture array approach contains 45 events (60%) using Gulkana data and 21 (81%) events using Greenland data.

5.2 HF Event Detection

Using the data from Gulkana, we detect 2,252 HF events of which 1456 (65%) made it to the final catalog (Figure 7a). We removed events that are either instrumental anomalies or have

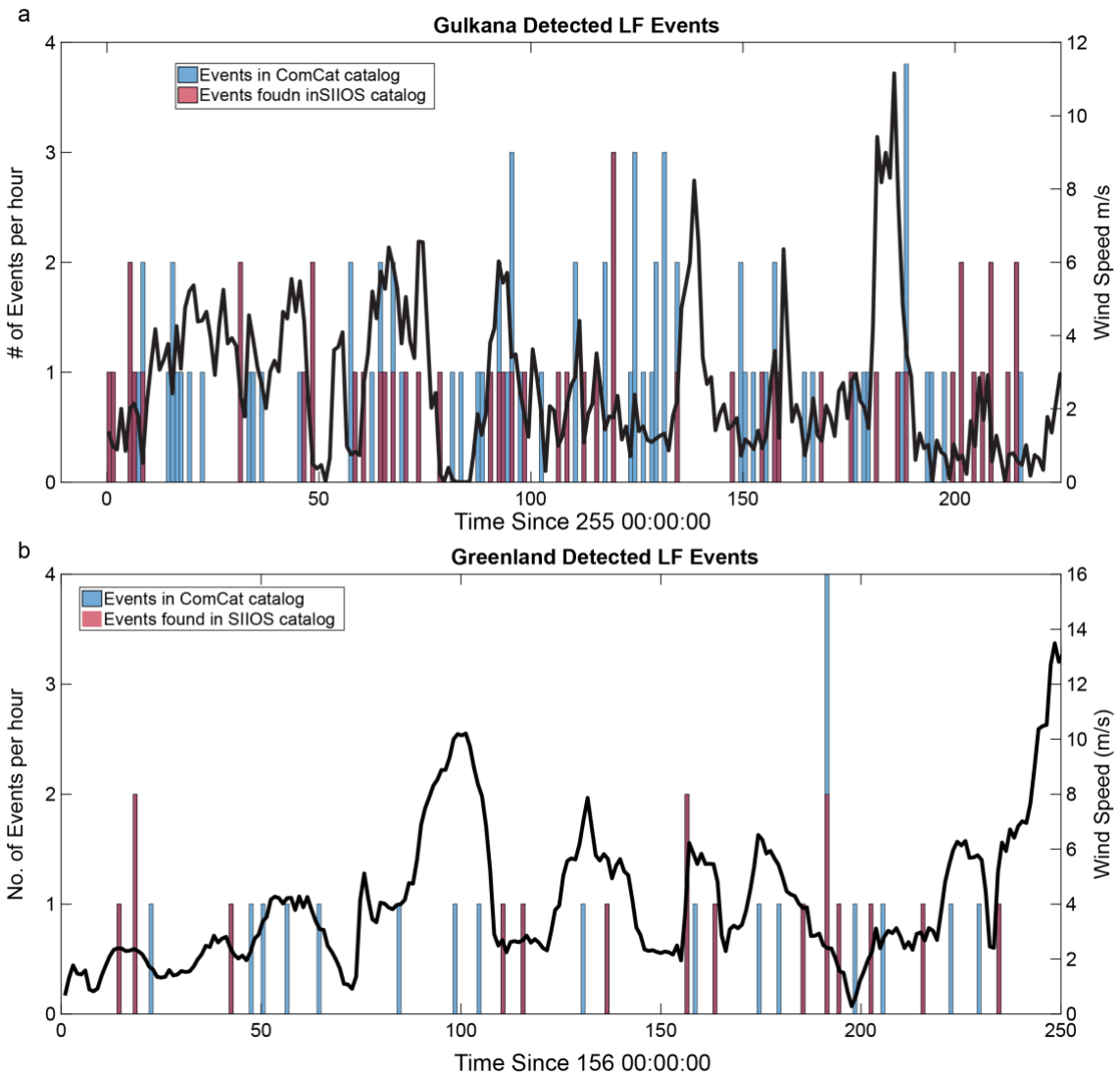

Figure 6. Comparison of Mw >5 or Epicentral Distances < 20° from the ComCat catalogs (blue) and the SIIOS automated detected catalog (red) for a) Gulkana and b) Greenland. A red color indicates the event was a positive detection. Many of the undetected ComCat events occurred when average hourly wind speeds exceed 4 m/s which would increase the measured background noise. A histogram value of 0 indicates no event occurred.

560 low signal-to-noise ratios (see methods section 3.1). Although the Gulkana Glacier HF events
561 appear to exhibit a diurnal signal, there is not a strong preference for local time occurrence. The
562 event catalog is compared to weather data from MERRA satellites (Global Modeling and
563 Assimilation Office (GMAO), 2015) and a local USGS weather station (Van Beusekom et al.,
564 2010). Although the events tend to coincide with increased temperature and changes in

565 temperature, occasionally, sharp rises in temperature are not indicative of detected events. These
566 occurrences tend to happen when wind speeds were particularly high (>20 mph).

567 Based on Pearson Correlation tests, however, the *r* value comparing number of detected
568 events per hour with temperature and changes with temperature are 0.2 and 0.19, respectively. The
569 corresponding *p* values are 0.003 and 0.006 (Benesty et al., 2009; Fisher, 1925). In order for a
570 correlation to be statistically significant, the *r* value should be close to 1, and the *p* value needs to
571 be less than 0.05. As this was not the case, temperature is not strongly correlated with the
572 occurrence of HF events. Given the short time duration of our experiment and the complex

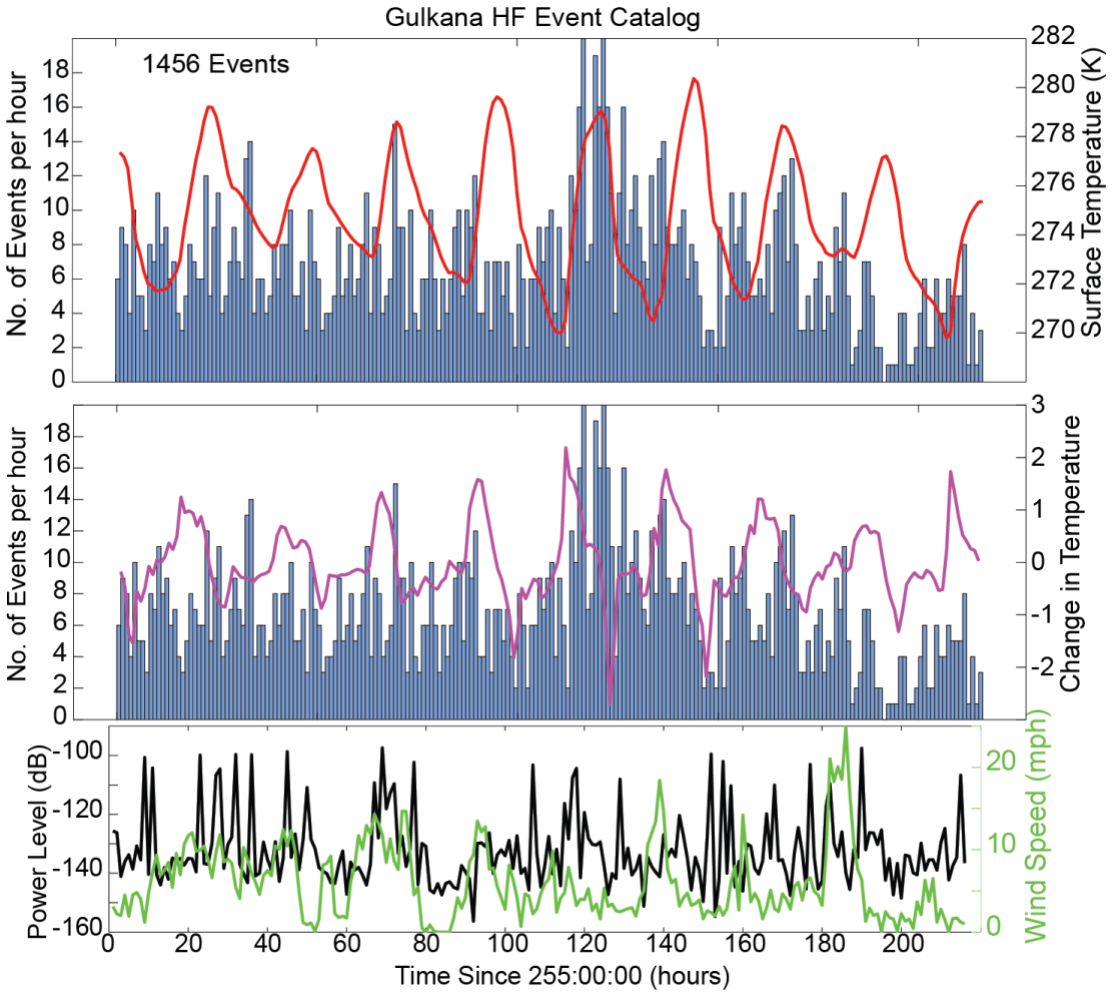

Figure 7. Comparison of number of detected events per hour (blue histogram) with a) temperature (K) (red), and b) change in temperature (purple). c) Wind speeds (green) and hourly averaged PDS background noise (black).

interactions of surface processes, however, we cannot exclude temperature as a driving mechanism for seismic events.

We use a polarization approach is used to determine the back azimuths to each HF event (Stachnik et al., 2012). Since it is difficult to distinguish between *P, S,* or surface waves, the entire waveform is used to determine back azimuths. Ideally, the *P* wave or surface waves alone would be used as these waves would have clear arrivals, thus the polarization across vertical and horizontal components would be clearer than using an entire waveform. At Gulkana Glacier, we have to apply a correction for station rotation at the Gulkana Glacier array; while no correction was needed for the northwest Greenland array. The reference station used at Gulkana Glacier (00A) was originally installed facing due north (0/360°). Upon demobilization, the final azimuth was recorded as 335°, indicating the instrument rotated 25° counterclockwise over the 2 weeks of the experiment. It is unknown if this rotation was constant, or occurred sporadically over the duration of the experiment, but we assume a constant rotation rate here. The recovered azimuth for

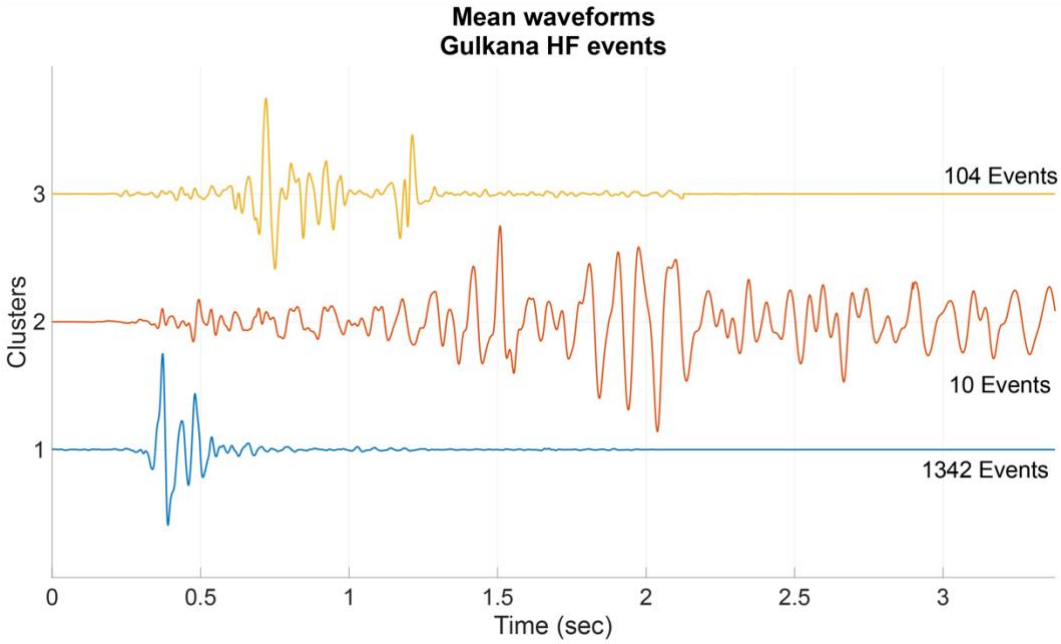

Figure 8. Mean waveforms from the HF event clusters analysis. Cluster 1 (blue) contained 1342 events; cluster 2 (red) had 10 events; cluster 3 (yellow) had 104 events.

each event is adjusted by computing the duration from the start time of the event and the start time of the station on 12 September 2017, and multiplying by 2.7° per day.

We perform a cluster analysis on the detected HF events to determine if there are any characteristics that could indicate their origin. For the Gulkana Glacier, there are 3 main categories (Figure 8). Here we plot the mean waveform (average value of the waveforms in each cluster in time) normalized by the maximum value of the mean waveform. The first cluster has the majority of the events (1342 events) and tend to originate with corrected back azimuths from between 150-180°, although there are events from nearly every direction. The waveforms in this cluster exhibit a single clear arrival. The events tend to dominate at high frequencies dominant either between 15-40 Hz or 40-70 Hz. HF Cluster 1 events occur during all times of day and are recorded throughout

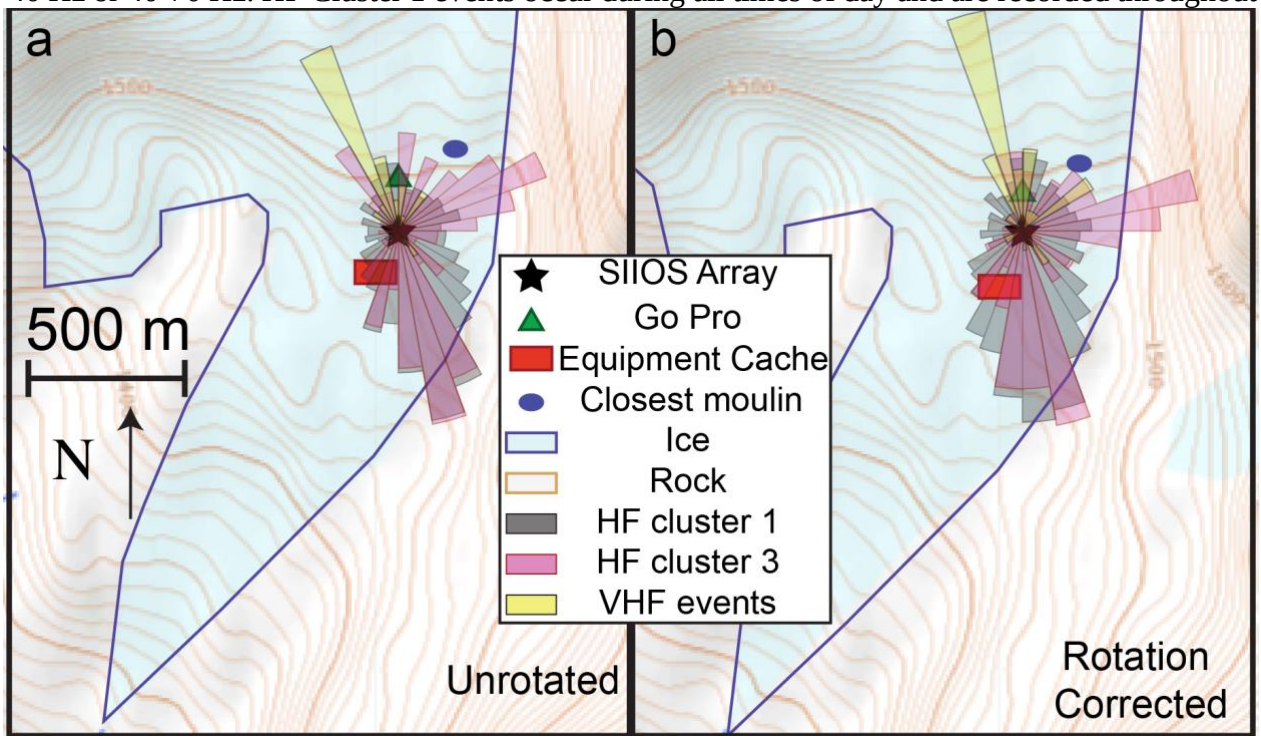

Figure 9. Map of Gulkana and SIIOS array (black star). The approximate locations of an equipment cache (red rectangle), Go Pro camera mounted on a pole (green triangle), and the closest moulin (blue oval) a) Uncorrected HF events back azimuths by cluster (grey, pink). b) After correcting for rotation. Topography maps are courtesy of the USGS (Gesch et al., 2009) where the blue shaded region is glacial ice and the brown shading is non-ice covered terrain. Darker lines in the topography map represent 100 m, while thinner line spacings are 10m. The rose diagrams are generated by finding the percentage of events that fall within 10º bins. The radius of each bin is then normalized by the maximum value of the cluster's rose diagram bins.

597 the passively recorded experiment. The southerly direction (back azimuths 150-180°) and duration

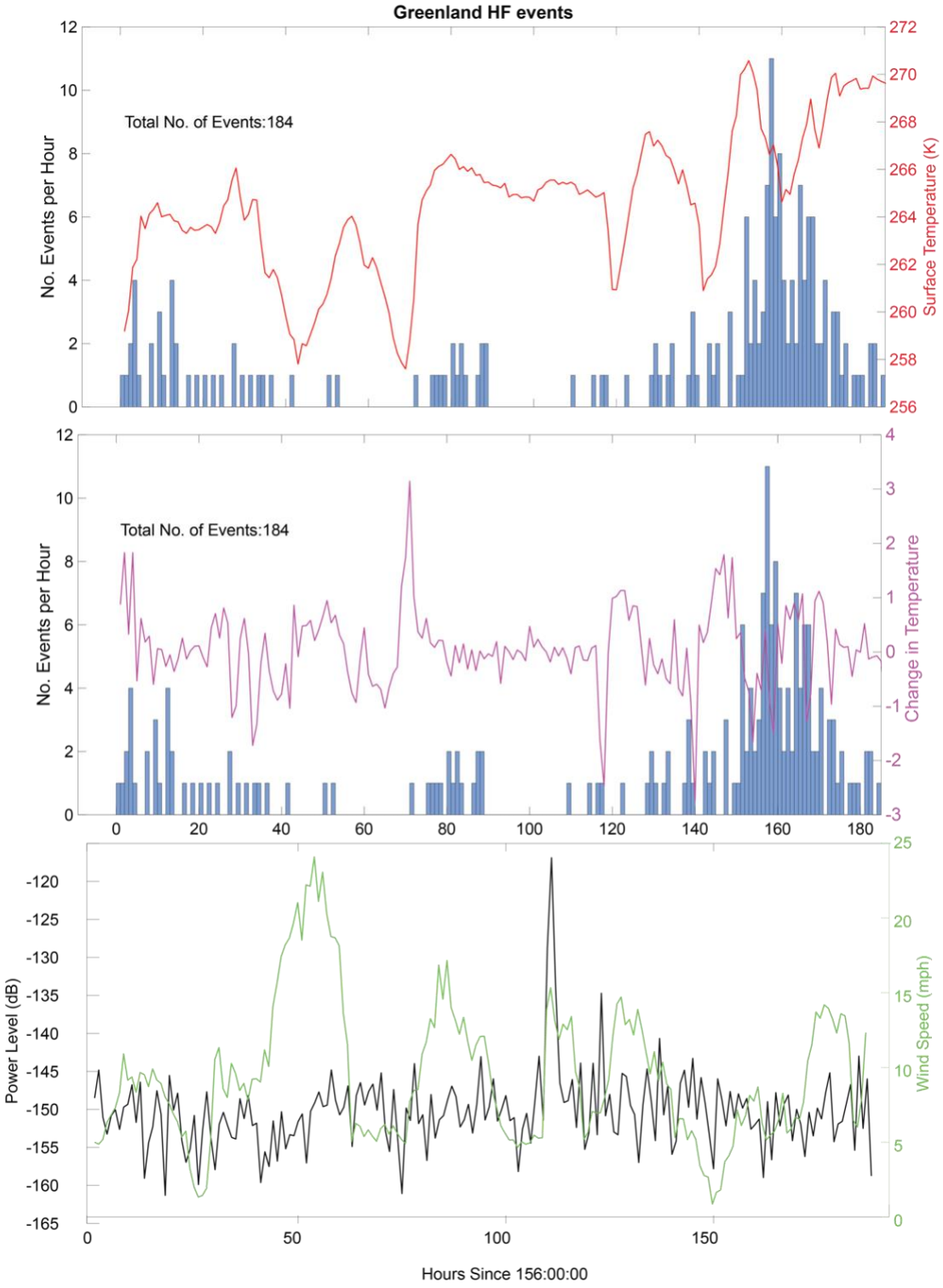

Figure 10. events detected at the Greenland (blue histogram) site versus surface temperature (red, top) and changes in temperature (purple, middle). The power level (black) is compared to wind speeds (green).

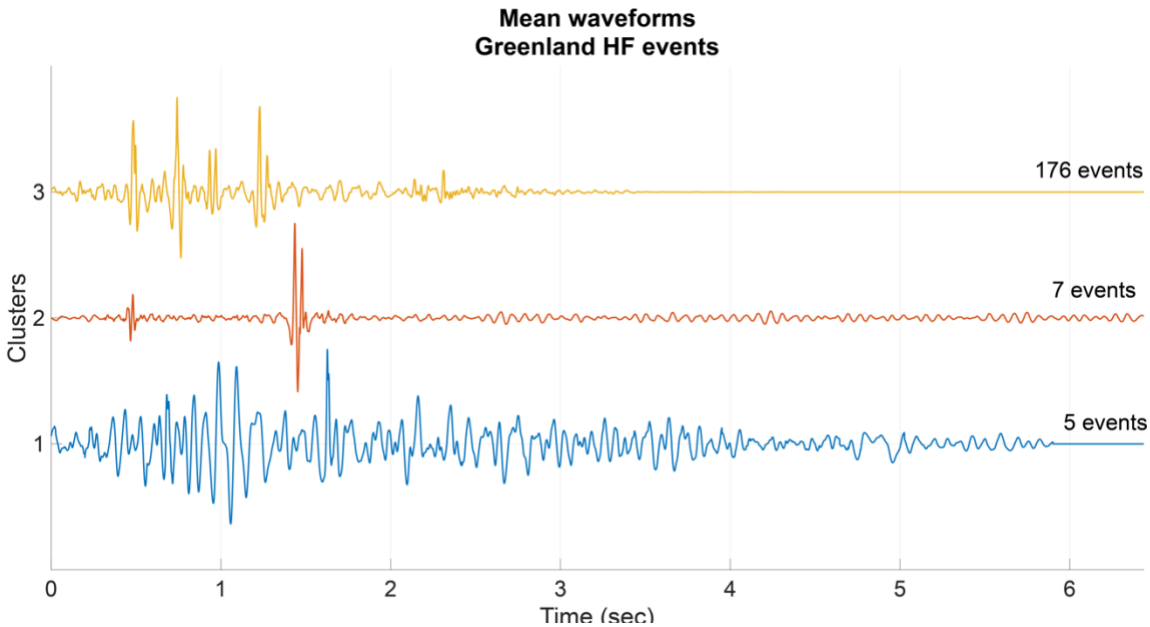

Figure 11. Greenland exhibited 3 clusters of events. The first cluster blue (1) had 5 events with low signal-to-noise ratios. The second cluster (red) had 7 events which tended to have higher signal-to-noise ratios. The third cluster (yellow) contained the majority of events. There were clear initial arrivals.

598 of events are consistent with events originating toward the ablation zone and terminus of the glacier
599 (Figure 9)(Gesch et al., 2009). The second cluster contains 10 events. These events have a
600 relatively small initial arrival with larger arrivals occurring within a second or two later. The events
601 originate from a wide range of back azimuths with no preferred direction suggesting their origins
602 came from a wide range of locations. They also occur throughout the experiment and at all times
603 of day. The final cluster has 104 events. Cluster 3 waveforms typically have a small initial arrival
604 followed by a larger arrival within 0.5 seconds. The events have back azimuths from all directions
605 but most occur either due south (150-180°) or due east (50-80°).

606 In Greenland, there were 1778 detected HF events in total of which 188 made it to the
607 final catalog. Almost 500 of the automated detections are due to instrument anomalies. These
608 instrument anomalies appear in the record primarily after 12 June 2018. For this reason, the catalog
609 stops at 11 June 2018 at about 20:00:00.000 when the last positive HF event is detected. Another
610 50 events are also removed from the initial catalog because they are associated with VHF events

discussed in the next section. Due to lower threshold for detection, the Greenland data tend to have noisier signals in the final catalog than Gulkana. Unlike the Gulkana events, there is no detectable diurnal signal (Figure 10) although most events tend to occur between 09:00 and 15:00 local time. The Greenland events fall into 3 clusters with 5 events falling into the first cluster (Figure 11). The first cluster has frequencies that dominate above 40 Hz. The events back azimuths indicate a southerly direction (Figure 12).

The second cluster contains only 7 events. The events resemble glitches due to high signal-to-noise ratios and a wide range of dominant frequencies. These events come from a wide range of azimuths and occur at all times of day.

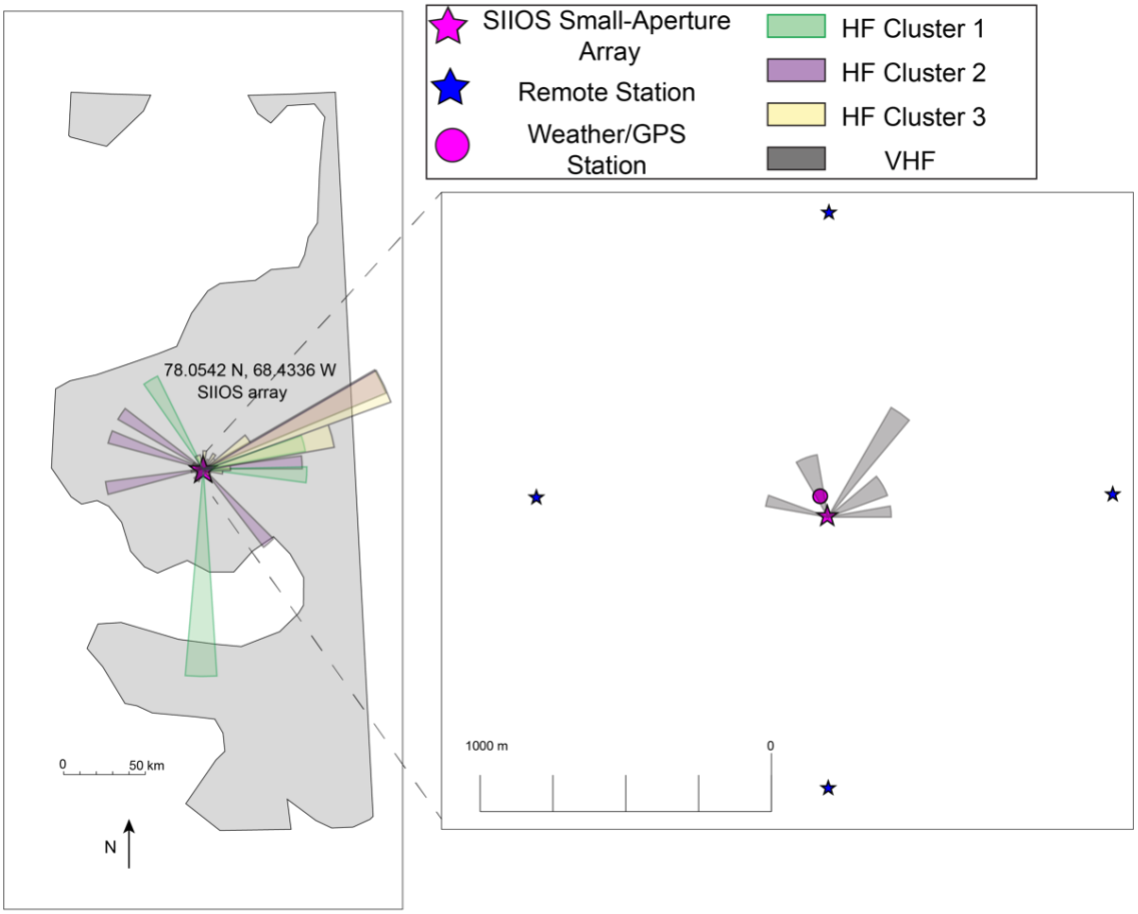

Figure 12. Map of SIIOS site in Greenland (purple star). In the left panel shaded gray indicates land versus ocean (white). Recovered azimuths of HF cluster 1 are shaded green, cluster 2 shaded purple and cluster 3 shaded yellow. The VHF events (grey) are plotted relative to remote stations (blue star) the center of the small-aperture array (purple star) and the GPS and weather stations (pink circle).

The third and final cluster consists of 176 events preferentially occur between the hours of 09:00-16:00 UTC (06:00-13:00 local). The events occur throughout the experiment, but most occur after 08 June 2018. The dominant frequencies are always below 20 Hz. The majority of the events have azimuths spanning 50-70°.

5.3 VHF Anomalies

During the inspection of HF events, a VHF signal was detected at both the Gulkana Glacier and northwest Greenland stations. We use a template detector to attempt to detect more of these VHF events. The initial autodetected catalog of VHF events contains 210 time series for Greenland of which 13 are included in the final catalog, Gulkana's final catalog contains 34 events out of ~2000 initial detections. The events that we removed were either noise or did not meet the repeating waveform pattern or exhibit the desired spectral characteristics.

As the waveforms are all similar to one another, a cluster analysis is not performed. For the Greenland field site, the duration of the series of events in the final catalog are typically only a few seconds long, although they could reach up to 10 seconds in length. Each of these detections contains several of the individual signals which individually last around a tenth of second. Many of the events occur toward the end of the Greenland experiment with most occurring on 09 June 2018. The events tend to occur between 08:00-09:00 UTC, (04:00-05:00 local). The events tend to occur during periods of low wind when environmental noise was also low. Most of the detections have low signal-to-noise ratios which made azimuth recovery difficult. Using the highest quality events, such as the time period used for the template, recovers azimuths pointed directly north. In order to test if the signal is originating from within the small-array, we also use remote station data to determine if those stations also record the VHF events. We could only use

3 out of the 4 remote stations because the southernmost station did not record useable data due to equipment malfunction. Each remote station records different back azimuths of the signal.

A similar signal is found in the Gulkana data. A template of the events was created and used to search for additional events in the dataset set. About 2000 VHF candidate events are found through the initial template detector of which 34 are in the final catalog. The majority of the events occur on 15 September 2017 between 04:00 and 06:00 UTC (20:00-22:00 local time). This time periods are all at night local time when temperatures were low and wind speeds were low (<5 m/s). The time series when the VHF are detected does not coincide with tectonic activity or high-rates of HF detections suggesting the VHF are not related to tectonic or HF activity. As with the Greenland VHF events, a cluster analysis is not performed among waveforms. Most of the events are several seconds long. The dominant frequency is between 380-400 Hz with additional resonances around 250 Hz and 125 Hz. After correcting for rotation effects, the events tend to originate from azimuths spanning 340-350°, and 50-60°.

Because these signals are within the human audible spectrum, we convert a subset of these signals from both Greenland and Gulkana to audio for interpretation, this allows us to attempt to identify their possible sources.

6 Discussion

6.1 Low Frequency Detections

As expected, the low-frequency events detected by our arrays coincide with regional and tectonic activity captured by other seismic stations and appear in standard event catalogs. Both single-station and small-aperture array approaches are able to detect multiple LF events. Operator inspection of the data yields the largest catalog but automated detections are still effective at

identifying a large number of events. Also, as expected, the small-aperture array is more reliable in eliminating false positive detections compared to the single-station automated detection algorithm. The small-aperture array algorithm rarely detects glitches; the majority of the detected LF events not in the ComCat catalog are local events such as thermal icequakes, moulin activity, or rockfalls. Because of the double detection, this creates a redundancy between LF and HF detections, but still would meet the goal of detecting events.

Any detection algorithm will have some false-negatives and false-positive detections in comparison to the events in the ComCat catalog, because of differences in deployment locations, instrument in situ sensitivity, and detection methods; a single station will have more false positive detections than a similarly deployed array. Previous studies on single-station detection capabilities have also shown similar limitations. For example, the InSight MarsQuake Service (MQS) team created a blind test to determine how well a catalog could be built for Mars using InSight as a single-station. In that test, not every event was detected, even by the MQS team (van Driel et al., 2019). They show that operator inspection of the time-series and spectrograms allow for higher rates of detections than using only automated detections such as the STA/LTA approach. Furthermore, they illustrate that only high magnitude events ($> M_w$ 4.0) could be detected over a large range of distances resulting in the detection of about 50-60% of all events. Now that InSight has landed, there is a similar bias in event location, where many of the events occur at shorter distances and only the largest magnitude events have been detected beyond 75º (as of the writing of this manuscript) (Giardini et al., 2020; InSight Marsquake Service, 2021).

By an operator seismologist reviewing the data directly, both temporally and spectrally, we are able to determine instances when automated detections failed. Most of the failed detections are not visible in the data, as expected. This is due to high environmental noise compared to event

signal amplitude. For example, many of the small local events are obscured when they occur during the daylight hours when local environment noise, such as wind, rain, melt, fracture, or water movement, is high. For example, in our dataset, when winds are above 4 m/s, the tectonic events are difficult to detect. This phenomenon is not just restricted to just the dataset in this study. The InSight mission to Mars are able to detect more events during the evening hours than during the day when winds are increased (Giardini et al., 2020). Previous terrestrial studies on glaciers have also shown that microseismicity can affect the detection of other events (C. G. Carr et al., 2020). Carr et al., 2020 shows how modifications to the standard STA/LTA algorithm by using a noise-adaptive detector can improve detection and reduce bias in detection statistics.

Events that occur at large epicentral distances are also less likely to be detected as their energies are likely more attenuated, especially at higher frequencies. Further, smaller magnitude events can also be obscured by larger magnitude events because the larger events have longer durations. For example, the large Mw 7.1 event obscures smaller events that occur in the hour following the initial arrival. Also, small magnitude events tend to occur more often so their waveforms interfere with each other upon arrival, or it is difficult to identify the *P* wave onset. Occasionally it is difficult to determine which catalog event the signal originates from.

One additional complication with the automated detections is fine tuning the parameters used to initiate a detection. We are able to fine tune our parameters by visually inspecting the time-series and spectral data and then adjusting the parameters as we see fit. For a mission with a short time lifetime (few weeks), this may not be feasible because the time to receive and analyze the initial data and communicate parameter alterations back to the lander is too long compared to the lifetime of the mission. As evidenced by the Gulkana and Greenland sites, even with the same

710 STA/LTA windows, the threshold limit can also vary by an order of magnitude because of the
711 environmental noise.

712 A future geophysical mission should consider mission lifetime expectations and data
713 availability when creating automated detection algorithms. The mission's team needs to decide
714 whether it is more acceptable to detect small local events, or to focus the detection algorithm on
715 teleseismic or regional events. While a human seismologist inspecting the data directly is the best
716 way to detect all possible tectonic events, it is time consuming, however, it can ensure few events
717 are missed and eliminate false-positive detections. This human inspection may not be feasible if
718 the mission's lifetime or data volume prevents sending data collected at a higher sampling rate. In
719 these instances, the automated detections would allow for higher sampled data to be returned only
720 for plausible detections, reducing the data volume. Data from a small-array can also help confirm
721 detections and improve data quality as not all stations would likely experience instrumental
722 anomalies at the same time. A small array would help reduce false positives, further improving
723 data volumes. We recognize, however, that a small-array is more expensive and could involve a
724 more complex deployment than a single-station.

725 6.2 HF Detections

726 We compare HF events to local weather data to determine if changes in the environment
727 are driving the diurnal seismicity observed at Gulkana. Although Gulkana HF event times show a
728 periodicity, the signals are not be linked through direct correlation to air temperature or changes
729 in temperature; we infer, therefore that air temperature is at most a weak or indirect driver of
730 seismicity. Further, a lack of HF detections tend to happen when wind speeds are particularly
731 high (>20 mph), suggesting high environmental noise is responsible for reducing the detection
732 capabilities. Previous studies in Antarctica (Lombardi et al., 2019; Olinger et al., 2019) find

733 approximately 1 thermally-driven event detected per hour, as temperature decreases. Here, we find
734 the HF detection rates of about 1-2 per hour and 3-14 per hour at our Greenland and Gulkana sites,
735 respectively. However, the occurrence of these events is not linked to decreasing temperatures,
736 suggesting that other processes may be triggering HF events at Gulkana, especially. A key
737 distinction between these previous studies and ours is that the previous studies used datasets
738 spanning years and a wider range of temperatures (-35 to -5°C), while ours are only ~ 2 weeks
739 long and have more limited temperature ranges of -17 to -3°C at the Greenland site and -3 to 7°C
740 at the Gulkana site. Because our HF events have similar characteristics to the previous studies in
741 both time-series waveforms and spectral content, it is possible that some of the detected events are
742 caused by cooling and expansion of ice. However, not all of the detected HF events are likely
743 caused by this effect.

744 One potential interpretation of the HF events is that they are related to increased surface
745 and subsurface runoff as noise levels and event number tend to be higher during the daytime hours.
746 During installation of the Gulkana equipment, increased surface runoff was observed with
747 increasing temperatures. As temperatures rose above freezing the supraglacial streams became
748 active (in terms of runoff) and audible noise could be heard from nearby moulins. Studies on
749 surface runoff suggest increased activity corresponds with increasing temperatures (Carmichael et
750 al., 2012, 2015; MacAyeal et al., 2019). The typical event duration of HF events (~2 seconds)
751 matches fluid resonances observed in volcanic-glacier systems (Métaxian et al., 2003), although
752 the frequency content above 5 Hz suggests cracking. Our analysis of the directionality of the HF
753 events detected at Gulkana indicate they may originate farther the downslope (southward) in the
754 ablation zone of the glacier where melt and runoff increase and coalesce into larger streams.
755 Although Europa or some icy ocean worlds are unlikely to have surface runoff, there could be

tidally modulated water-ice interactions within the ice shells which could mimic the observed drainage events. For example, the tiger stripe features near Enceladus' southern pole may mimic drainage events as they open and close during the tidal cycle. Titan, which does have liquid hydrocarbons on the surface (Hayes et al., 2008; Mitri et al., 2007), could exhibit similar fluvial signals to those we observe.

Another possible source for HF events we identify at Gulkana is rockfall. During the installation, numerous rockfall events were heard and observed on the steep moraine slopes in close proximity to the glacier. Previous studies (Norris, 1994; V. Zimmer & Sitar, 2015) detected rockfalls using similar filters and STA/LTA parameters to those chosen for our HF event detector. These studies also show that rockfalls occurring within a kilometer should be detectable on a broadband seismometer. We interpret our cluster 3 in the Gulkana catalog as rockfall because they originate from the direction of greatest topography changes for the nearby slopes (topographic data from Gesch et al., 2009) (Figure 9). On icy ocean worlds, there could be analogous signals from ice breaking near rifting zones or locally high topography. As the ice breaks, gravity may pull ice chunks apart creating ice falls or debris flows.

The HF detection algorithm for the Greenland deployment finds only one tenth of the number of events detected at Gulkana. The Greenland catalog also fails to show correlation between occurrence rate and surface temperature ($r=0.348$, $p=1.23*10^{-6}$) or changes in temperature ($r=-0.112$, $p=0.132$). Although the recovered azimuths suggest an easterly origin, there is a 180° ambiguity to the events. If the events do occur due west, that is the direction of the nearest coastline. The signal quality of the Greenland HF events is not as high as Gulkana and it is difficult for a stack to produce a clear mean signal for each cluster (Figure 8). One reason the events at Greenland are noisier could be due to the local wind speeds. High winds coincide with increased

779 environmental noise (Figure 10), which reduces the ability to detect events. Previous studies have
780 shown that the 5-15 Hz seismic range can be particularly affected by wind speeds (Dybing et al.,
781 2019). Another reason for the low quality of the HF events is that they tend to occur further away
782 from the stations than the HF events at the Gulkana field site; this reduces the magnitude overall
783 and attenuates the higher frequency components of the signal, both of which will make the events
784 harder to detect.

785 Two key differences between Gulkana and Greenland are the quantity and quality of HF
786 events. With respect to quantity of the HF events, the difference stems from the different geologic
787 settings. The SIIOS site on Gulkana is within the ablation zone, while the SIIOS site in Greenland
788 is situated in the accumulation zone, far from the ablation zone. Proximity within the ablation zone
789 where melt and related surface processes are active increases the number of detectable events
790 because less energy is lost due to geometrical spreading and attenuation. Our findings indicate a
791 single-station or small-array deployed on an icy ocean world will likely be able to detect the diurnal
792 influences of local events and determine the direction from which the events originate. Defining
793 the direction and detecting diurnal frequency on an icy ocean world will help constrain the
794 mechanisms driving local seismicity and regions of high activity. If, however, the goals of the
795 mission are more global in scale, then detection of LF events would become a priority. In that
796 instance, a landing site more analogous to Greenland would be more appropriate as the reduction
797 in local HF events could help improve the detection of LF events.

798 6.3 VHF Detections (> 20 Hz)

799 In the VHF frequency range, the most distinctive signal we find is a repeating signal that
800 is common to both sites. We detect this signal through implementing a template detector. Due to
801 the high frequency, repetition, and regularity of the signal, we suspect cultural (anthropogenic)

sources or a nearby natural source(s). For example, poles and equipment left in the field can have harmonic seismic signatures that resemble the seismic signatures of moulins (Carmichael, 2019). In addition, previous studies (Allstadt & Malone, 2014) have shown that repeating signals could be due to snow loading. To try and identify the events and distinguish the source of their origin, we study the repeating nature of the signals, short reoccurrence rate, VHF content, and event durations characteristics.

We can reasonably rule out moulins for the Greenland dataset, as no active moulins were present near the field site at the time of deployment and because the site is near the ice divide and in the accumulation zone, a moulin or surface stream of any kind are rare and nonexistent at this time. At the Gulkana Glacier site, moulins are prevalent and very likely to contribute to the VHF noise, but they are unlikely to be the cause of the repeating signal common to both sites. Moulins are known to cause fracturing that exhibit HF energy and have short durations(Carmichael et al., 2015) as well as VHF tremor (Roeoesli et al., 2016). The fracturing due to moulins is more likely to contribute to the HF (<20 Hz) diurnal signals we observe, the VHF signal from moulin tremor is typically emergent and therefore not detectable by our algorithm. Moulins can be conclusively ruled out as a potential source for the Greenland site as none were present at the site and conditions are too cold for them to form (no surface melt). At Gulkana, moulins are likely to have contributed to some of the HF and VHF signals and environmental noise, but they cannot explain the repeating nature and very short duration of the most distinctive VHF signals.

Snow loading and firn quakes can create high frequency signals with repetitive signals(Lough et al., 2015). While snow and firn loading may be a viable source for some VHF signals detected at the Greenland site, only small patches of saturated firn existed at the Gulkana site, and therefore this source is unlikely a contributing signal at the Gulkana site. The Greenland

site did accumulate ~1 meter of snow, but Gulkana did not see significant precipitation (< 10 cm of snow). Furthermore, the previous studies (Allstadt & Malone, 2014; Lough et al., 2015) note the repeating signals had a reoccurrence rate of several minutes, not tenths of seconds and the frequency content of the repeating events was 1-5 Hz.

We also consider installation equipment as a source of the VHF signals. For example, a hard drive spinning or clicking, settling of equipment as the snow or ice underneath compacts or melts, or wind interaction with the lander, nearby tarps, and flags. For the northwest Greenland site, the signal is detected by both the small-aperture array and the remote array 1 km away; therefore, we can rule out sources unique to only the small-aperture array as the remote stations also record the signal. Previous studies in the cryosphere found that poles left in the field as markers could create high frequency signals (Carmichael, 2019). At both the small-aperture array and remote stations, bamboo poles were left in the field in order to help locate the stations. Polarization analysis of the signals also indicate that the remote stations point in different directions, likely due to the different positioning of the poles relative to the station. We listened to longer duration seismograms (from day 09 June 2018 around 12:00 UTC), and determine that the signal is most similar to wind blowing past flexible bamboo poles or flags flapping in wind gusts. To rule out signals caused by approaching helicopters, we also listened to seismogram time-series when helicopters were known to be in the vicinity. While there are similarities between the signal generated by the helicopters, there are differences. The characteristic spectra of the events also help to identify these slight differences between helicopter signals and wind-driven pole vibrations. The similarities exist because the helicopters generate wind that also cause poles to move as if there was a strong natural wind. The helicopter almost certainly activated pole resonances as the rotor wash created considerable wind in the vicinity of the experiment. The

dominant frequency of the events (Figure 3c) provide further evidence. The bamboo poles were approximately 1-2 meters in height above the snow. The 4th harmonic for a 1-meter cylinder with one fixed end is roughly 320 Hz, the same as the characteristic frequency of the signal. The corresponding first harmonic is 80 Hz, which does appear on spectrograms. We conclude that it is likely the VHF signals recorded at the Greenland site are caused by the poles moving in the wind. It is noted that when the winds were at the highest, these events are not detected. Visual inspection of the time-series data confirm that no events occur during periods of high winds (>10 m/s). It is possible the winds are strong enough to cause the other sources of environmental noise to increase or are strong enough to force the poles to stop swaying.

At Gulkana there were no bamboo poles, however there was a cache of equipment left at the field site that was covered with tarp and a pole with a GoPro camera attached to it. This pole was located due north of the small-array and the equipment cache was due south of the array. Although the tarp was secured with tie lines, it was still able to flap from wind gusts. The back azimuths of the VHF events tend point in the direction of 330-350° (due north). This direction is towards a nearby GoPro camera setup, and notably not a common azimuth for most HF detections (Figure 10). As with the data recorded at the Greenland site, we listened to the seismograms to help identify possible sources. The signals sound like a semi-regular thump. We compare these signals to other environmental noise without the repeating signals to verify that the thumping noise is only heard when VHF events were recorded. The other environmental signals sound like blowing wind or static without any thumping or flapping noises. Based on this evidence we believe the VHF signals detected by our algorithm are caused by a combination the poles, flags, and tarps left behind during deployment.

The detections of this equipment-induced VHF signal indicates the importance of having the capability to distinguish signal sources to prevent attributing spacecraft-generated noise to natural local noise sources. At both Greenland and Gulkana, equipment left in the field created sources that obscured other local, naturally occurring, events. Previous planetary missions have also detected instrumental and spacecraft influences on seismic signals. The Apollo missions recorded astronaut movements (Khatib et al., 2020; Nakamura, 1976), the only true anthropogenic signals detected on another object in the solar system. Thermal moonquakes have also been associated with the Lunar Exploration Module and other equipment left on the lunar surface (Weber et al., 2018) long after the astronauts left the surface. The InSight mission on Mars has numerous signals originating from the lander (Giardini et al., 2020). While future missions may not have bamboo poles, flags, or tarps, the missions may include other instrumentation that can generate seismic signals, including solar panel arrays, instrument booms, landing equipment, and lander deck and legs. Titan, in particular does have an atmosphere which could produce wind and produce similar signals to those we observed. Although more analogous to deep ocean currents, Titan's atmosphere can produce wind noise (Lorenz et al., 2021). It will be vital for future missions to determine whether signals are from landers, or if the events have a natural origin that can be used to characterize the local environment.

6.4 Summary

For future missions to icy ocean worlds, expected seismicity and science goals should be considered carefully when determining a landing site. Based on our findings we have the following recommendations:

1. A small-aperture array outperforms a single-station. While a single-station is effective, a small-aperture array provides redundancy in case of equipment failure, leads to

893 increases in positive detections while reducing false positives, and provides additional
894 information to identify sources (especially local environmental signals).
895 2. Potential landing sites will vary in terms of local seismic activity.
896 a. If local activity is the primary science goals, then begin close to a potentially
897 active region will increase the number of local events and may help characterize
898 the activity along an active area such as a fault, chaos terrain, or nearby
899 cryovolcanism. A lack of detected activity may then indicate the area
900 surrounding the landing is no longer active or less active than predicted.
901 b. If recovering global structure or seismicity is the primary goal, a quieter site is
902 more optimal. A site farther from local activity will liekly detect a higher
903 percentage of larger magnitude tectonic events. This may be preferred if the
904 goals of the mission are to investigate larger scale structure or global-scale
905 activity rather than a specific feature.
906 c. A balance between these two goals may be achievable with more sophisticated
907 automated detection algorithms (e.g. C. G. Carr et al., 2020).
908 3. If mission lifetime or data transfer is limited, an automated detection algorithm will be
909 critical. Operator searches find the most events, but requires large data volumes and
910 more time-consuming searches.
911 4. Regardless of the site selected or detection method, the character of the environmental
912 noise may vary in time an cause bias in the temporal interpretation event counts and
913 magnitudes (C. G. Carr et al., 2020)

914 In the case of Europa, where the high levels of radiation would reduce the mission lifetime
915 to a few weeks, we recommend a landing site near a potentially active area. Such a landing

site will have a better chance of detecting events to characterize the local ice dynamic environment and possibly the global structure from teleseismic events. We recommend a more sophisticated noise-adaptive automated detection algorithm to find potential events and send back higher sampling rate data for events with a range of magnitudes along with some spectral data characterizing the environmental noise through time. For a mission to Enceladus or Titan where a mission may survive years, a landing site in a quieter area may be more suitable. Larger events would be more likely to be detected due to decreased environmental noise; the extended time would allow for more detailed analysis of events on a range of scales as well as the environmental noise. Operator inspection would likely find the most events.

7 Conclusions

The SIIOS analog sites provide data to investigate how single-station seismometers and small-aperture arrays can detect and identify sources of seismicity on an icy ocean world. Our study highlights the diversity of sources that would be recorded by a future seismic experiment on an icy ocean world mission and emphasizes that a range of LF and HF signal types are likely to exist in these environments. Our experiments show that geophysical missions to an icy ocean world should expect to record large teleseismic or regional events, but not ignore the possibility of local events generated by active ice dynamics as well as lander-generate seismicity. In addition to naturally occurring sources, future missions would need to determine if spacecraft sources are likely to add noise to the mission.

In our study, equipment-generated noise appears most strongly in VHF events are detected at both sites, namely noise generated by marker poles, flags, and tarps interacting with the wind. Future analog experiments and missions should be aware of possible anthropogenic/cultural

939 signals and take steps to mitigate them. While these signals may be used to constrain near-surface
940 structure, they add to environmental noise and obscured naturally occurring signals.

941 We suggest that a single-station seismometer is capable of detecting numerous teleseismic
942 and regional events at an icy ocean world landing site, and a large-scale network is not needed to
943 achieve fundamental seismology science objectives. Previous terrestrial studies indicate similar
944 capability (Bose et al., 2017; Frohlich & Pulliam, 1999; Panning et al., 2015), and it has been
945 demonstrated on Mars (Khan et al., 2021; Knapmeyer-Endrun et al., 2021; Stähler et al., 2021) but
946 we expand on these studies by using identical instrumentation deployments in two different icy
947 ocean world analog environments.

948 The HF and VHF events reveal characteristics of the geological and tectonic environment.
949 HF events at Gulkana are numerous and may contribute to overall higher environmental noise
950 measured by our instruments. The HF events at Gulkana are likely due to crevasse opening, most
951 likely near the glacier terminus, as well as meltwater or rainfall runoff. Some of the events are
952 consistent with by nearby rockfalls and mass wasting. The Greenland site HF data is also far noisier
953 than the Gulkana data despite general lower levels of environmental noise at these frequencies.
954 Increased wind at Greenland could have increased the environmental noise. The signal strength
955 may have also been decreased due to attenuation and geometrical spreading if the events occurred
956 at greater distances than those at Gulkana.

957 Not only do we test single-station capabilities, but we are also able to quantify a small-
958 aperture array designed to mimic a robotic deployment. The setups on Gulkana and in Greenland
959 further allow us to quantify capabilities in high activity and low activity locations. Despite high
960 levels of local environmental noise at the Gulkana site, distant tectonic events are detected with
961 the single-station. The small-aperture arrays further improved our ability to detect more events and

962 distinguish events from instrumental anomalies. In a noisier environment, the small-aperture array
963 would help eliminate false detections caused by instrumental anomalies. The reduction of false
964 positives would help ensure only true events were sent back at higher sampling rates, improving
965 the overall science return. Although the small-aperture array approach produces more detections,
966 many of the detections made at Gulkana are from local events not tectonic events, creating
967 redundancy among the detection algorithm settings. Since the local events can still yield
968 information regarding the local environment, it may be preferred to have more data from any
969 natural event, than risk not detecting events to reduce false positives from glitches.

970 Future geophysical missions will need to assess the goals and limitations of the spacecraft
971 when deciding on landing sites and whether to rely on a single-station and/or automated detection
972 approaches. Small aperture-arrays have the potential to improve the science return and are able to
973 more robustly identify events without seismologist review, but also increase the data volume.
974 Automated detections can help reduce data volume when time is limited, but a seismologist
975 inspection will lead to more detections of LF events. A low noise site may lead to the detection of
976 more LF events, but is highly dependent upon the likelihood of larger magnitude more distant
977 events. For shorter lived experiments, a site close to a seismically active region may detect higher
978 quality and quantity of HF events that can help characterize the local environment, and underlying
979 icy ocean world structure.

980

981

982 **Acknowledgments and Data**

983 This project was supported by NASA PSTAR Grant #80NSSC17K0229 and NASA
984 NESSF # 80NSSC18K1260. Although AGM was employed by JPL at the time of submission, this

work was done as a private venture and not in the author's capacity as an employee of the Jet Propulsion Laboratory, California Institute of Technology.

SIIOS data used in this study can be obtained from the Incorporated Research Institutions for Seismology (IRIS) Data Management Center (DMC) with network code YH (2017) and doi: 10.7914/SN/ YH_2017 for Gulkana and network code 9C (2018) and DOI: 10.7914/SN/9C_2018 for the Greenland data. Maps and previous data on Gulkana are available through the U.S. Geological Survey (USGS; https://alaska.usgs.gov/portal/project.php?project_id=108). Plate boundaries were mapped using open-source code (Shure, 2020) and data from (Argus et al., 2011) Gulkana weather data are available at https:// waterdata.usgs.gov/ak/nwis/uv?site_no=15478038. Python code for PPSDS, STA/LTA, and Coincidence triggers were generated using the open-source project, ObsPy (Beyreuther et al., 2010). The reference catalog was built using the USGS ComCat web service provided by the ANSS. The catalog of events detected by SIIOS is available using: https://drum.lib.umd.edu/handle/1903/26478 (currently only has LF events, but HF events will be added by publication).

We thank the IRIS PASSCAL facility at the Instrument Center at New Mexico Tech, especially Pnina Miller and Noël Barstow, for providing training on instruments and lending equipment to the project. We also thank Polar Field Services, Susan Detweiler, J. Bella Brodbeck, Chris Carr, Ferderico Covi, Namrah Habib, Andrew Johnson, and Emilie Sinkler for their assistance in field logistics.

References

Allstadt, K., & Malone, S. D. (2014). Swarms of repeating stick-slip icequakes triggered by snow loading at Mount Rainier volcano. *Journal of Geophysical Research: Earth Surface, 119*(5), 1180–1203. https://doi.org/10.1002/2014JF003086

Amundson, J. M., Clinton, J. F., Fahnestock, M., Truffer, M., Luthi, M. P., & Motyka, R. J. (2012). Observing calving-generated ocean waves with coastal broadband seismometers,

Jakobshavn Isbrae, Greenland. *Annals of Glaciology*, *53*(60), 79–84. https://doi.org/10.3189/2012/AoG60A200

Ardhuin, F., Stutzmann, E., Schimmel, M., & Mangeney, A. (2001). Ocean wave sources of seismic noise. *Journal of Geophysical Research: Oceans*, *116*(C9). https://doi.org/10.1029/2011JC006952

Argus, D. F., Gordon, R. G., & DeMets, C. (2011). Geologically current motion of 56 plates relative to the no-net-rotation reference frame. *Geochemistry, Geophysics, Geosystems*, *12*(11). https://doi.org/10.1029/2011GC003751

Baer, M., & Kradolfer, U. (1987). An automatic phase picker for local and teleseismic events. *Bulletin of the Seismological Society of America*, *77*(4), 1437–1445.

Baker, E. H., O'Neel, S., Fagre, D. B., Whorton, E. N., Sass, L. C., McNeil, C. J., et al. (2018). USGS Benchmark Glacier Mass Balance and Project Data: 1966-2016: U.S. Geological Survey data release. https://doi.org/10.5066/F7BG2N8R

Banfield, D., Spiga, A., Newman, C., Forget, F., Lemmon, M., Lorenz, R., et al. (2020). The atmosphere of Mars as observed by InSight. *Nature Geoscience*, *13*(3), 190–198. https://doi.org/10.1038/s41561-020-0534-0

Barnes, J. W., Turtle, E. P., Trainer, M. G., Lorenz, R. D., MacKenzie, S. M., Brinckerhoff, W. B., et al. (2021). Science Goals and Objectives for the Dragonfly Titan Rotorcraft Relocatable Lander. *Planetary Science Journal*, *in press*(4), 130. https://doi.org/10.3847/PSJ/abfdcf

Benesty, J., Chen, J., Huang, Y., & Cohen, I. (2009). Pearson correlation coefficient. In *Noise reduction in speech processing* (pp. 1–4). Springer.

Van Beusekom, A. E., O'Neel, S. R., March, R. S., Sass, L. C., & Cox, L. H. (2010). *Re-analysis of Alaskan Benchmark Glacier Mass-Balance Data Using the Index Method Scientific Investigations Report 2010-5247*. Retrieved from http://www.usgs.gov/pubprod

Beyreuther, M., Barsch, R., Krischer, L., Megies, T., Behr, Y., & Wassermann, J. (2010). ObsPy: A Python Toolbox for Seismology. *Seismological Research Letters*, *81*(3), 530–533. https://doi.org/10.1785/gssrl.81.3.530

Bierhaus, E. B., Zahnle, K., Chapman, C. R., Pappalardo, R. T., McKinnon, W. R., & Khurana, K. K. (2009). Europa's crater distributions and surface ages. *Europa*, 161–180.

Billings, S. E., & Kattenhorn, S. A. (2005). The great thickness debate: Ice shell thickness models for Europa and comparisons with estimates based on flexure at ridges. *Icarus*, *177*(2), 397–412. https://doi.org/10.1016/j.icarus.2005.03.013

Bland, M. T., & McKinnon, W. B. (2017). Breaking the shell: Initiating plate tectonic-like subduction on Europa. In *AAS/Division for Planetary Sciences Meeting Abstracts* (Vol. 49).

Bose, M., Clinton, J. F., Ceylan, S., Euchner, F., van Driel, M., Khan, A., et al. (2017). A probabilistic framework for single-station location of seismicity on Earth and Mars. *Physics of the Earth and Planetary Interiors*, *262*, 48–65. https://doi.org/10.1016/j.pepi.2016.11.003

Bouquet, A., Mousis, O., Waite, J. H., & Picaud, S. (2015). Possible evidence for a methane source in Enceladus' ocean. *Geophysical Research Letters*, *42*(5), 1334–1339.

https://doi.org/doi:10.1002/2014GL063013

Bowling, J. S., Livingstone, S. J., Sole, A. J., & Chu, W. (2019). Distribution and dynamics of Greenland subglacial lakes. *Nature Communications*, *10*(1), 2810. https://doi.org/10.1038/s41467-019-10821-w

Bulow, R. C., Johnson, C. L., Bills, B. G., & Shearer, P. M. (2007). Temporal and spatial properties of some deep moonquake clusters. *Journal of Geophysical Research: Planets*, *112*(9), 1–12. https://doi.org/10.1029/2006JE002847

Carmichael, J. D. (2019). Narrowband signals recorded near a moulin that are not moulin tremor: a cautionary short note. *Annals of Glaciology*, *60*(79), 231–237. https://doi.org/10.1017/aog.2019.23

Carmichael, J. D., Pettit, E. C., Hoffman, M., Fountain, A., & Hallet, B. (2012). Seismic multiplet response triggered by melt at Blood Falls, Taylor Glacier, Antarctica. *Journal of Geophysical Research: Earth Surface*, *117*(F3). https://doi.org/10.1029/2011JF002221

Carmichael, J. D., Joughin, I., Behn, M. D., Das, S., King, M. A., Stevens, L., & Lizarralde, D. (2015). Seismicity on the western Greenland Ice Sheet: Surface fracture in the vicinity of active moulins. *Journal of Geophysical Research: Earth Surface*, *120*(6), 1082–1106. https://doi.org/10.1002/2014JF003398

Carr, C. G., Carmichael, J. D., Pettit, E. C., & Truffer, M. (2020). The influence of environmental microseismicity on detection and interpretation of small-magnitude events in a polar glacier setting. *Journal of Glaciology*, *66*(259), 790–806. https://doi.org/10.1017/jog.2020.48

Carr, M. H., Belton, M. J. S. S., Chapman, C. R., Davies, M. E., Geissler, P., Greenberg, R., et al. (1998). Evidence for a subsurface ocean on Europa. *Nature*, *391*(6665), 363–365. https://doi.org/10.1038/34857

Chouet, B. A. (1996). Long-period volcano seismicity: its source and use in eruption forecasting. *Nature*, *380*(6572), 309–316. https://doi.org/10.1038/380309a0

Clinton, J. F., Nettles, M., Walter, F., Anderson, K., Dahl-Jensen, T., Giardini, D., et al. (2014). Seismic network in Greenland monitors Earth and ice system. *Eos, Transactions American Geophysical Union*, *95*(2), 13–14.

Crary, A. P. (1955). A brief study of Ice Tremors. *Bulletin of the Seismological Society of America*, *45*(1), 1–9. Retrieved from https://pubs.geoscienceworld.org/ssa/bssa/article/45/1/1/115725/a-brief-study-of-ice-tremors

Crotwell, H. P., Owens, T. J., & Ritsema, J. (1999). The TauP Toolkit: Flexible Seismic Travel-time and Ray-path Utilities. *Seismological Research Letters*, *70*(2), 154–160. https://doi.org/10.1785/gssrl.70.2.154

Dawes, P. R. (2009). Precambrian–Palaeozoic geology of Smith Sound, Canada and Greenland: key constraint to palaeogeographic reconstructions of northern Laurentia and the North Atlantic region. *Terra Nova*, *21*(1), 1–13. https://doi.org/10.1111/j.1365-3121.2008.00845.x

van Driel, M., Ceylan, S., Clinton, J. F., Giardini, D., Alemany, H., Allam, A., et al. (2019). Preparing for InSight: Evaluation of the Blind Test for Martian Seismicity. *Seismological*

Research Letters, *90*(4), 1518–1534. https://doi.org/10.1785/0220180379

Duennebier, F., & Sutton, G. H. (1974). Thermal moonquakes. *Journal of Geophysical Research*, *79*(29), 4351–4363. https://doi.org/10.1029/JB079i029p04351

Dybing, S. N., Ringler, A. T., Wilson, D. C., & Anthony, R. E. (2019). Characteristics and Spatial Variability of Wind Noise on Near-Surface Broadband Seismometers. *Bulletin of the Seismological Society of America*, *109*(3), 1082–1098. https://doi.org/10.1785/0120180227

Dziewonski, A. M., & Anderson, D. L. (1981). Preliminary Reference Earth Model. *Physics of the Earth and Planetary Interiors*, *25*(4), 297–356. https://doi.org/10.1016/0031-9201(81)90046-7

Ewing, M., Crary, A. P., & Thorne, A. M. J. (1934). Propagation of elastic waves in ice. Part II. *Physics*, *5*(7), 181–184. https://doi.org/10.1063/1.1745249

Fan, G., & Wallace, T. (1991). The determination of source parameters for small earthquakes from a single, very broadband seismic station. *Geophysical Research Letters*, *18*(8), 1385–1388. https://doi.org/10.1029/91GL01804

Fisher, R. A. (1925). *Statistical methods for research workers*. *London: Oliver and Loyd, Ltd* (13th ed.).

Forghani-Arani, F., Behura, J., Haines, S. S., & Batzle, M. (2013). An automated cross-correlation based event detection technique and its application to a surface passive data set. *Geophysical Prospecting*, *61*(4), 778–787. https://doi.org/10.1111/1365-2478.12033

Frohlich, C., & Pulliam, J. (1999). Single-station location of seismic events: a review and a plea for more research. *Physics of the Earth and Planetary Interiors*, *113*(1–4), 277–291. https://doi.org/10.1016/S0031-9201(99)00055-2

Gesch, D., Evans, G., Mauck, J., Hutchinson, J., & Carswell Jr, W. J. (2009). The national map—Elevation. *US Geological Survey Fact Sheet*, *3053*(4).

Giardini, D., Lognonné, P., Banerdt, W. B., Pike, W. T., Christensen, U., Ceylan, S., et al. (2020). The seismicity of Mars. *Nature Geoscience*, *13*(3), 205–212. https://doi.org/10.1038/s41561-020-0539-8

Global Modeling and Assimilation Office (GMAO). (2015). MERRA-2 tavg1_2d_slv_Nx: 2d,1-Hourly,Time-Averaged,Single-Level,Assimilation,Single-Level Diagnostics V5.12.4,. https://doi.org/10.5067/VJAFPLI1CSIV

Greeley, R., Figueredo, P. H., Williams, D. A., Chuang, F. C., Klemaszewski, J. E., Kadel, S. D., et al. (2000). Geologic mapping of Europa. *Journal of Geophysical Research-Planets*, *105*(E9), 22559–22578. https://doi.org/10.1029/1999je001173

Greeley, R., Chyba, C. F., Head, J. W., McCord, T., McKinnon, W. B., Pappalardo, R. T., & Figueredo, P. H. (2004). Geology of Europa. *Jupiter: The Planet, Satellites and Magnetosphere*, 329–362.

Greenberg, R., Hoppa, G. V., Tufts, B. R., Geissler, P., Riley, J., & Kadel, S. (1999). Chaos on Europa. *Icarus*, *141*(2), 263–286. https://doi.org/10.1006/icar.1999.6187

Greenberg, R., Hoppa, G. V., Bart, G., & Hurford, T. A. (2003). Tidal stress patterns on Europa's crust. *Celestial Mechanics & Dynamical Astronomy*, *87*(1–2), 171–188.

https://doi.org/10.1023/A:1026169424511

Hand, K. P., Chyba, C. F., Priscu, J. C., Carlson, R. W., & Nealson, K. H. (2009). Astrobiology and the potential for life on Europa. *Europa*, 589–629.

Hand, K. P., Murray, A. E., Garvin, J. B., Brinckerhoff, W. B., Christner, B. C., Edgett, K. S., et al. (2017). *Report of the Europa Science Definition Team*. Retrieved from https://europa.nasa.gov/resources/58/europa-lander-study-2016-report/

Hayes, A., Aharonson, O., Callahan, P., Elachi, C., Gim, Y., Kirk, R., et al. (2008). Hydrocarbon lakes on Titan: Distribution and interaction with a porous regolith. *Geophysical Research Letters*, *35*(9), L09204. https://doi.org/10.1029/2008GL033409

Hendrix, A. R., Hurford, T. A., Barge, L. M., Bland, M. T., Bowman, J. S., Brinckerhoff, W., et al. (2018). The NASA Roadmap to Ocean Worlds. *Astrobiology*, *19*(1), 1–27. https://doi.org/10.1089/ast.2018.1955

Hoppa, G. V., Tufts, B. R., Greenberg, R., & Geissler, P. (1999). Strike-slip faults on Europa: Global shear patterns driven by tidal stress. *Icarus*, *141*(2), 287–298. https://doi.org/10.1006/icar.1999.6185

Hurford, T. A., Sarid, A. R., Greenberg, R., & Bills, B. G. (2009). The influence of obliquity on europan cycloid formation. *Icarus*, *202*(1), 197–215. https://doi.org/10.1016/j.icarus.2009.02.036

Hurford, T. A., Henning, W. G., Maguire, R., Lekic, V., Schmerr, N. C., Panning, M. P., et al. (2020). Seismicity on tidally active solid-surface worlds. *Icarus*, *338*, 113466. https://doi.org/10.1016/j.icarus.2019.113466

Iess, L., Rappaport, N. J., Jacobson, R. A., Racioppa, P., Stevenson, D. J., Tortora, P., et al. (2010). Gravity field, shape, and moment of inertia of Titan. *Science*, *327*(5971), 1367–1369. https://doi.org/10.1126/science.1182583

Iess, L., Stevenson, D. J., Parisi, M., Hemingway, D., Jacobson, R. A., Lunine, J. I., et al. (2014). The Gravity Field and Interior Structure of Enceladus. *Science*, *344*(6179), 78–80. https://doi.org/10.1126/science.1250551

InSight Marsquake Service. (2021). Mars Seismic Catalogue, InSight Mission; V6 2021-04-01. ETHZ, IPGP, JPL, ICL, MPS, Univ. Bristol. https://doi.org/10.12686/a11

Isanina, E. V, Krupnova, N. A., Popov, S. V, Masolov, V. N., & Lukin, V. V. (2009). Deep structure of the Vostok Basin, East Antarctica as deduced from seismological observations. *Geotectonics*, *43*(3), 221–225. https://doi.org/10.1134/S0016852109030042

Jiménez, E., Cara, M., & Rouland, D. (1989). Focal mechanisms of moderate-size earthquakes from the analysis of single-station three-component surface-wave records. *Bulletin of the Seismological Society of America*, *79*(4), 955–972.

Johnson, B. C., Sheppard, R. Y., Pascuzzo, A. C., Fisher, E. A., & Wiggins, S. E. (2017). Porosity and Salt Content Determine if Subduction Can Occur in Europa's Ice Shell. *Journal of Geophysical Research: Planets*, *122*(12), 2765–2778. https://doi.org/10.1002/2017JE005370

Kattenhorn, S. A., & Prockter, L. M. (2014). Evidence for subduction in the ice shell of Europa.

Nature Geoscience, *7*(10), 762–767. https://doi.org/10.1038/ngeo2245

Katterhorn, S. A., & Hurford, T. A. (2009). Tectonics of Europa. In R. Pappalardo, W. B. McKinnon, & K. Khurana (Eds.), *Europa* (pp. 199–236). The University of Arizona Press.

Kawamura, T., Lognonné, P., Nishikawa, Y., & Tanaka, S. (2017). Evaluation of deep moonquake source parameters: Implication for fault characteristics and thermal state. *Journal of Geophysical Research: Planets*, *122*(7), 1487–1504. https://doi.org/10.1002/2016JE005147

Khan, A., van Driel, M., Bose, M., Giardini, D., Ceylan, S., Yan, J., et al. (2016). Single-station and single-event marsquake location and inversion for structure using synthetic Martian waveforms. *Physics of the Earth and Planetary Interiors*, *258*, 28–42. https://doi.org/10.1016/j.pepi.2016.05.017

Khan, A., Ceylan, S., van Driel, M., Giardini, D., Lognonné, P., Samuel, H., et al. (2021). Upper mantle structure of Mars from InSight seismic data. *Science*, *373*(6553), 434–438. https://doi.org/10.1126/science.abf2966

Khatib, A. S., Schmerr, N. C., Feist, B., Plescia, J. B., & Petro, N. E. (2020). Active-Source Seismology from anthropogenic sources during th Apollo 11 Lunar Mission. In *Lunar and Planetary Science Conference*. Retrieved from http://apolloinrealtime.org/11/?t=107:08:20.

Khurana, K. K., Kivelson, M. G., Stevenson, D. J., Schubert, G., Russell, C. T., Walker, R. J., & Polanskey, C. (1998). Induced magnetic fields as evidence for subsurface oceans in Europa and Callisto. *Nature*, *395*(6704), 777–780. https://doi.org/10.1038/27394

Kieffer, S. W. (1984). Seismicity at Old Faithful Geyser: an isolated source of geothermal noise and possible analogue of volcanic seismicity. *Journal of Volcanology and Geothermal Research*, *22*(1–2), 59–95. https://doi.org/10.1016/0377-0273(84)90035-0

Kim, S. G., Kraeva, N., & Chen, Y.-T. (2000). Source parameter determination of regional earthquakes in the Far East using moment tensor inversion of single-station data. *Tectonophysics*, *317*(1–2), 125–136. https://doi.org/10.1016/S0040-1951(99)00274-7

Knapmeyer-Endrun, B., Panning, M. P., Bissig, F., Joshi, R., Khan, A., Kim, D., et al. (2021). Thickness and structure of the martian crust from InSight seismic data. *Science*, *373*(6553), 438–443. https://doi.org/10.1126/science.abf8966

Kovach, R. L., & Watkins, J. S. (1973). The structure of the lunar crust at the Apollo 17 site. In *Lunar and Planetary Science Conference Proceedings* (Vol. 4, p. 2549).

Lee, S., Zanolin, M., Thode, A. M., Pappalardo, R. T., & Makris, N. C. (2003). Probing Europa's interior with natural sound sources. *Icarus*, *165*(1), 144–167. https://doi.org/10.1016/S0019-1035(03)00150-7

Lombardi, D., Gorodetskaya, I., Barruol, G., & Camelbeeck, T. (2019). Thermally induced icequakes detected on blue ice areas of the East Antarctic ice sheet. *Annals of Glaciology*, *60*(79), 45–56. https://doi.org/10.1017/aog.2019.26

Lopes, R. M. C., Kirk, R. L., Mitchell, K. L., LeGall, A., Barnes, J. W., Hayes, A., et al. (2013). Cryovolcanism on Titan: New results from Cassini RADAR and VIMS. *Journal of Geophysical Research: Planets*, *118*(3), 416–435. https://doi.org/10.1002/jgre.20062

Lorenz, R. D., Panning, M. P., Stähler, S., Shiraishi, H., Yamada, R., Turtle, E. P., et al. (2019). Titan Seismology with Dragonfly: Probing the Internal Structure of the Most Accessible Ocean World. *50th Lunar and Planetary Science Conference*, *57*(763), Abstract #2173. Retrieved from http://www.lpi.usra.edu/meetings/lpsc2019/pdf/2173.pdf

Lorenz, R. D., Shiraishi, H., Panning, M., & Sotzen, K. (2021). Wind and surface roughness considerations for seismic instrumentation on a relocatable lander for Titan. *Planetary and Space Science*, *206*, 105320. https://doi.org/10.1016/j.pss.2021.105320

Lough, A. C., Barcheck, C. G., Wiens, D. A., Nyblade, A., & Anandakrishnan, S. (2015). A previously unreported type of seismic source in the firn layer of the East Antarctic Ice Sheet. *Journal of Geophysical Research: Earth Surface*, *120*(11), 2237–2252. https://doi.org/10.1002/2015JF003658

MacAyeal, D. R., Wang, Y. T., & Okal, E. A. (2015). Ambient seismic, hydroacoustic, and flexural gravity wave noise on a tabular iceberg. *Journal of Geophysical Research-Earth Surface*, *120*(2), 200–211. https://doi.org/10.1002/2014jf003250

MacAyeal, D. R., Banwell, A. F., Okal, E. A., Lin, J., Willis, I. C., Goodsell, B., & MacDonald, G. J. (2019). Diurnal seismicity cycle linked to subsurface melting on an ice shelf. *Annals of Glaciology*, *60*(79), 137–157. https://doi.org/10.1017/aog.2018.29

Mackenzie, S. M., Neveu, M., Davila, A. F., Lunine, J. I., Craft, K. L., Cable, M. L., et al. (2021). The Enceladus Orbilander Mission Concept : Balancing Return and Resources in the Search for Life. *The Planetary Science Journal*, *2*(2), 77. https://doi.org/10.3847/PSJ/abe4da

Maguire, R., Schmerr, N., Pettit, E., Riverman, K., Gardner, C., Della-Giustina, D., et al. (2021). Geophysical constraints on the properties of a subglacial lake in northwest Greenland. *The Cryosphere Discussions*, 1–19. https://doi.org/10.5194/tc-2020-321

Manchee, E. B., & Weichert, D. H. (1968). Epicentral uncertainties and detection probabilities from the Yellowknife seismic array data. *Bulletin of the Seismological Society of America*, *58*(5), 1359–1377.

March, R. S. (2000). *Mass balance, meteorological, ice motion, surface altitude, runoff, and ice thickness data at Gulkana glacier, Alaska, 1995 balance year*. Fairbanks, AK. https://doi.org/Water-Resources Investigations Report 00-4074

March, R. S., & Trabant, D. C. (1997). *Mass Balance, Meteorological, Ice Motion, Surface Altitude, and Runoff Data at Gulkana Glacier, Alaska, 1993 Balance Year*. https://doi.org/Water-Resources Investigations Report 96-429

Marusiak, A. G., Schmerr, N. C., DellaGiustina, D. N., Pettit, E. C., Dahl, P. H., Avenson, B., et al. (2020). The Deployment of the Seismometer to Investigate Ice and Ocean Structure (SIIOS) on Gulkana Glacier, Alaska. *Seismological Research Letters*, *91*(3), 1901–1914. https://doi.org/10.1785/0220190328

Marusiak, A. G., Vance, S. D., Panning, M. P., Běhounková, M., Byrne, P. K., Choblet, G., et al. (2021). Exploration of Icy Ocean Worlds Using Geophysical Approaches. *The Planetary Science Journal*, *2*(4), 150. https://doi.org/10.3847/PSJ/ac1272

Marusiak, A. G., Schmerr, N. C., DellaGiustina, D. N., Avenson, B., Bailey, S. H., Bray, V. J., et

al. (2021). The Deployment of the Seismometer to Investigate Ice and Ocean Structure (SIIOS) in Northwest Greenland: An Analog Experiment for Icy Ocean World Seismic Deployments. *Seismological Research Letters*. https://doi.org/10.1785/0220200291

Matsuyama, I., Beuthe, M., Hay, H. C. F. C., Nimmo, F., & Kamata, S. (2018). Ocean tidal heating in icy satellites with solid shells. *Icarus*, *312*, 208–230. https://doi.org/10.1016/j.icarus.2018.04.013

McCord, T. B., Hansen, G. B., Matson, D. L., Johnson, T. V, Crowley, J. K., Fanale, F. P., et al. (1999). Hydrated salt minerals on Europa's surface from the Galileo near-infrared mapping spectrometer (NIMS) investigation. *Journal of Geophysical Research-Planets*, *104*(E5), 11827–11851. https://doi.org/10.1029/1999je900005

McNamara, D. E., & Buland, R. (2004). Ambient Noise Levels in the Continental United States. *Bulletin of the Seismological Society of America*, *94*(4), 1517–1527. https://doi.org/10.1785/012003001

McNutt, S. R., & Roman, D. C. (2015). Volcanic Seismicity. *The Encyclopedia of Volcanoes*, 1011–1034. https://doi.org/10.1016/B978-0-12-385938-9.00059-6

Métaxian, J.-P., Araujo, S., Mora, M., & Lesage, P. (2003). Seismicity related to the glacier of Cotopaxi Volcano, Ecuador. *Geophysical Research Letters*, *30*(9). https://doi.org/10.1029/2002GL016773

Meyer, J., & Wisdom, J. (2007). Tidal heating in Enceladus. *Icarus*, *188*(2), 535–539. https://doi.org/10.1016/j.icarus.2007.03.001

Mitri, G., Showman, A. P., Lunine, J. I., & Lorenz, R. D. (2007). Hydrocarbon lakes on Titan. *Icarus*, *186*(2), 385–394. https://doi.org/10.1016/j.icarus.2006.09.004

Mordret, A., Mikesell, T. D., Harig, C., Lipovsky, B. P., & Prieto, G. A. (2016). Monitoring southwest Greenland's ice sheet melt with ambient seismic noise. *Science Advances*, *2*(5), e1501538. https://doi.org/10.1126/sciadv.1501538

Nakamura, Y. (1976). Seismic energy transmission in the lunar surface zone determined from signals generated by movement of lunar rovers. *Bulletin of the Seismological Society of America*, *66*(2), 593–606. Retrieved from https://pubs.geoscienceworld.org/ssa/bssa/article/66/2/593/117549/seismic-energy-transmission-in-the-lunar-surface

National Research Council. (2003). *New Frontiers in Solar System Exploration*. Washington, DC: The National Academies Press. https://doi.org/10.17226/10898

Nimmo, F., & Gaidos, E. (2002). Strike-slip motion and double ridge formation on Europa. *Journal of Geophysical Research: Planets*, *107*(E4). https://doi.org/10.1029/2000JE001476

Nimmo, F., & Pappalardo, R. T. (2016). Ocean worlds in the outer solar system. *Journal of Geophysical Research: Planets*, *121*(8), 1378–1399. https://doi.org/10.1002/2016JE005081@10.1002/(ISSN)2169-9100.JGRE25

Nimmo, F., & Schenk, P. (2006). Normal faulting on Europa: implications for ice shell properties. *Journal of Structural Geology*, *28*(12), 2194–2203. https://doi.org/10.1016/j.jsg.2005.08.009

Nimmo, F., Giese, B., & Pappalardo, R. T. (2003). Estimates of Europa's ice shell thickness from elastically-supported topography. *Geophysical Research Letters*, *30*(5). https://doi.org/Artn 1233 10.1029/2002gl016660

Norris, R. D. (1994). Seismicity of rockfalls and avalanches at three Cascade Range volcanoes: implications for seismic detection of hazardous mass movements. *Bulletin - Seismological Society of America*, *84*(6), 1925–1939. https://doi.org/10.1016/0148-9062(95)99022-p

O'Brien, D. P., Geissler, P., & Greenberg, R. (2002). A melt-through model for chaos formation on Europa. *Icarus*, *156*(1), 152–161. https://doi.org/10.1006/icar.2001.6777

Olinger, S. D., Lipovsky, B. P., Wiens, D. A., Aster, R. C., Bromirski, P. D., Chen, Z., et al. (2019). Tidal and Thermal Stresses Drive Seismicity Along a Major Ross Ice Shelf Rift. *Geophysical Research Letters*, *46*(12), 6644–6652. https://doi.org/10.1029/2019GL082842

Olsen, K. G., Hurford, T. A., Schmerr, N. C., Huang, M., Brunt, K. M., Zipparo, S., et al. (2021). Projected Seismic Activity at the Tiger Stripe Fractures on Enceladus, Saturn from an Analog Study of Tidally Modulated Icequakes within the Ross Ice Shelf, Antarctica. *Journal of Geophysical Research: Planets*, 1–18. https://doi.org/10.1029/2021je006862

Ostenso, N. A., Sellmann, P. V., & Péwé, T. L. (1965). The Bottom Topography of Gulkana Glacier, Alaska Range, Alaska. *Journal of Glaciology*, *5*(41), 651–660. https://doi.org/10.3189/S0022143000018669

Palmer, S. J., Dowdeswell, J. A., Christoffersen, P., Young, D. A., Blankenship, D. D., Greenbaum, J. S., et al. (2013). Greenland subglacial lakes detected by radar. *Geophysical Research Letters*, *40*, 6154–6159. https://doi.org/10.1002/2013GL058383

Panning, M. P., Lekic, V., Manga, M., Cammarano, F., & Romanowicz, B. (2006). Long-period seismology on Europa: 2. Predicted seismic response. *Journal of Geophysical Research: Planets*, *111*(E12), n/a-n/a. https://doi.org/10.1029/2006JE002712

Panning, M. P., Beucler, E., Drilleau, M., Mocquet, A., Lognonne, P., & Banerdt, W. B. (2015). Verifying single-station seismic approaches using Earth-based data: Preparation for data return from the InSight mission to Mars. *Icarus*, *248*, 230–242. https://doi.org/10.1016/j.icarus.2014.10.035

Pappalardo, R. T., Belton, M. J. S., Breneman, H. H., Carr, M. H., Chapman, C. R., Collins, G. C., et al. (1999). Does Europa have a subsurface ocean? Evaluation of the geological evidence. *Journal of Geophysical Research: Planets*, *104*(E10), 24015–24055. https://doi.org/10.1029/1998je000628

Paranicas, C., Mauk, B. H., Khurana, K., Jun, I., Garrett, H., Krupp, N., & Roussos, E. (2007). Europa's near-surface radiation environment. *Geophysical Research Letters*, *34*(15). https://doi.org/10.1029/2007GL030834

Parkinson, C. D., Liang, M.-C., Yung, Y. L., & Kirschivnk, J. L. (2008). Habitability of Enceladus: Planetary Conditions for Life. *Origins of Life and Evolution of Biospheres*, *38*(4), 355–369. https://doi.org/10.1007/s11084-008-9135-4

Perrin, C., Rodriguez, S., Jacob, A., Lucas, A., Spiga, A., Murdoch, N., et al. (2020). Monitoring of Dust Devil Tracks Around the InSight Landing Site, Mars, and Comparison With In Situ Atmospheric Data. *Geophysical Research Letters*, *47*(10).

https://doi.org/10.1029/2020GL087234

Peters, L. E., Anandakrishnan, S., Holland, C. W., Horgan, H. J., Blankenship, D. D., & Voigt, D. E. (2008). Seismic detection of a subglacial lake near the South Pole, Antarctica. *Geophysical Research Letters*, *35*(23), L23501. https://doi.org/10.1029/2008GL035704

Peterson, J. (1993). *Observations and modeling of seismic background noise*. Albuquerque, New Mexico: US Geological Survey Albuquerque. https://doi.org/10.3133/ofr93322 Open-File Report 93-322

Podolskiy, E. A., & Walter, F. (2016). Cryoseismology. *Reviews of Geophysics*, *54*(4), 708–758. https://doi.org/10.1002/2016RG000526

Porco, C. C., Helfenstein, P., Thomas, P. C., Ingersoll, A. P., Wisdom, J., West, R., et al. (2006). Cassini observes the active south pole of Enceladus. *Science*, *311*(5766), 1393–1401. https://doi.org/10.1126/science.1123013

Prockter, L. M., Pappalardo, R. T., & Head, J. W. (2000). Strike-slip duplexing on Jupiter's icy moon Europa. *Journal of Geophysical Research: Planets*, *105*(E4), 9483–9488. https://doi.org/10.1029/1999JE001226

Quick, L. C., Barnouin, O. S., Prockter, L. M., & Patterson, G. W. (2013). Constraints on the detection of cryovolcanic plumes on Europa. *Planetary and Space Science*, *86*, 1–9. https://doi.org/10.1016/J.PSS.2013.06.028

Raulin, F. (2008). Astrobiology and habitability of Titan. In *Strategies of Life Detection* (pp. 37–48). Springer.

Reynolds, R. T., Squyres, S. W., Colburn, D. S., & McKay, C. P. (1983). On the habitability of Europa. *Icarus*, *56*(2), 246–254. https://doi.org/10.1016/0019-1035(83)90037-4

Rhoden, A. R., Wurman, G., Huff, E. M., Manga, M., & Hurford, T. A. (2012). Shell tectonics: A mechanical model for strike-slip displacement on Europa. *Icarus*, *218*(1), 297–307. https://doi.org/10.1016/j.icarus.2011.12.015

Rhoden, A. R., Hurford, T. A., Roth, L., & Retherford, K. (2015). Linking Europa's plume activity to tides, tectonics, and liquid water. *Icarus*, *253*, 169–178. https://doi.org/10.1016/j.icarus.2015.02.023

Roberts, J. H., & Nimmo, F. (2008). Tidal heating and the long-term stability of a subsurface ocean on Enceladus. *Icarus*, *194*(2), 675–689. https://doi.org/10.1016/j.icarus.2007.11.010

Roeoesli, C., Walter, F., Ampuero, J.-P., & Kissling, E. (2016). Seismic moulin tremor. *Journal of Geophysical Research: Solid Earth*, *121*(8), 5838–5858. https://doi.org/10.1002/2015JB012786

Roth, L., Saur, J., Retherford, K. D., Strobel, D. F., Feldman, P. D., McGrath, M. A., & Nimmo, F. (2014). Transient Water Vapor at Europa's South Pole. *Science*, *343*(6167), 171–174. https://doi.org/10.1126/science.1247051

Schmidt, B. E., Blankenship, D. D., Patterson, G. W., & Schenk, P. M. (2011). Active formation of 'chaos terrain' over shallow subsurface water on Europa. *Nature*, *479*(7374), 502–505. https://doi.org/10.1038/nature10608

Schubert, G., Anderson, J. D., Spohn, T., & McKinnon, W. B. (2004). Interior composition,

structure and dynamics of the Galilean satellites. *Jupiter: The Planet, Satellites and Magnetosphere*, *1*, 281–306.

Schubert, G., Anderson, J. D., Travis, B. J., & Palguta, J. (2007). Enceladus: Present internal structure and differentiation by early and long-term radiogenic heating. *Icarus*, *188*(2), 345–355. https://doi.org/10.1016/J.ICARUS.2006.12.012

Schubert, G., Sohl, F., & Hussmann, H. (2009). Interior of europa. *Europa*, 353–367.

Showman, A. P., & Han, L. J. (2005). Effects of plasticity on convection in an ice shell: Implications for Europa. *Icarus*, *177*(2), 425–437. https://doi.org/10.1016/j.icarus.2005.02.020

Shure, L. (2020). MATLAB® for Analyzing and Visualizing Geospatial Data. MATLAB Central File Exchange.

Smith, P. H. (1980). The radius of Titan from Pioneer Saturn data. *Journal of Geophysical Research*, *85*(A11), 5943. https://doi.org/10.1029/JA085iA11p05943

Sohl, F., Spohn, T., Breuer, D., & Nagel, K. (2002). Implications from Galileo observations on the interior structure and chemistry of the Galilean satellites. *Icarus*, *157*(1), 104–119. https://doi.org/10.1006/icar.2002.6828

Sohl, F., Choukroun, M., Kargel, J., Kimura, J., Pappalardo, R. T., Vance, S. D., & Zolotov, M. (2010). Subsurface Water Oceans on Icy Satellites: Chemical Composition and Exchange Processes. *Space Science Reviews*, *153*(1–4), 485–510. https://doi.org/10.1007/s11214-010-9646-y

Sotin, C., Head, J. W., & Tobie, G. (2002). Europa: Tidal heating of upwelling thermal plumes and the origin of lenticulae and chaos melting. *Geophysical Research Letters*, *29*(8), 74. https://doi.org/10.1029/2001GL013844

Sotin, C., Tobie, G., Wahr, J., & McKinnon, W. B. (2009). Tides and TIdal Heating on Europa. In R. Pappalardo, W. B. McKinnon, & K. Khurana (Eds.), *Europa* (pp. 85–118). The University of Arizona Press.

Stachnik, J. C., Sheehan, A. F., Zietlow, D. W., Yang, Z., Collins, J., & Ferris, A. (2012). Determination of New Zealand Ocean Bottom Seismometer Orientation via Rayleigh-Wave Polarization. *Seismological Research Letters*, *83*(4), 704–713. https://doi.org/10.1785/0220110128

Stähler, S. C., Panning, M. P., Vance, S. D., Lorenz, R. D., van Driel, M., Nissen-Meyer, T., et al. (2017). Seismic Wave Propagation in Icy Ocean Worlds. *Journal of Geophysical Research: Planets*, *123*(1), 206–232. https://doi.org/10.1002/2017JE005338

Stähler, S. C., Panning, M. P., Hadziioannou, C., Lorenz, R. D., Vance, S., Klingbeil, K., & Kedar, S. (2019). Seismic signal from waves on Titan's seas. *Earth and Planetary Science Letters*, *520*, 250–259. https://doi.org/10.1016/j.epsl.2019.05.043

Stähler, S. C., Khan, A., Banerdt, W. B., Lognonné, P., Giardini, D., Ceylan, S., et al. (2021). Seismic detection of the martian core. *Science*, *373*(6553), 443–448. https://doi.org/10.1126/science.abi7730

The National Academy of the Sciences. (2011). *Visions and Voyages for Planetary Science in*

the Decade 2013-2022. (N. R. C. of the N. Academies, Ed.). Washington, D.C.: The National Academy of Sciences. https://doi.org/10.17226/13117

Trnkoczy, A. (1999). Topic Understanding and parameter setting of STA/LTA trigger algorithm. *New Manual of Seismological Observatory Practice*, *2*, 1–20. https://doi.org/10.2312/GFZ.NMSOP-2_IS_8.1

Tufts, B. R., Greenberg, R., Hoppa, G., & Geissler, P. (1999). Astypalaea Linea: A Large-Scale Strike-Slip Fault on Europa. *Icarus*, *141*(1), 53–64. https://doi.org/10.1006/icar.1999.6168

Tyler, R. H. (2008). Strong ocean tidal flow and heating on moons of the outer planets. *Nature*, *456*(7223), 770–772. https://doi.org/10.1038/nature07571

U.S. Geological Survey, E. H. P. (2020). Advanced National Seismic System (ANSS) Comprehensive Catalog of Earthquake Events and Products. https://doi.org/0.5066/F7MS3QZH

US Geological Survey. (2020). National Water Information System (USGS Water Data for the Nation). Retrieved August 1, 2020, from https://nwis.waterdata.usgs.gov/ak/nwis/uv?cb_00020=on&cb_00035=on&cb_00036=on&cb_00052=on&cb_61728=on&cb_72194=on&format=gif_default&site_no=15478038&period=&begin_date=2017-09-08&end_date=2017-09-23

Vance, S. D., Panning, M. P., Stähler, S., Cammarano, F., Bills, B. G., Tobie, G., et al. (2018). Geophysical Investigations of Habitability in Ice-Covered Ocean Worlds. *Journal of Geophysical Research: Planets*, *123*(1), 180–205. https://doi.org/10.1002/2017JE005341

Vance, S. D., Kedar, S., Panning, M. P., Stähler, S. C., Bills, B. G., Lorenz, R. D., et al. (2018). Vital Signs: Seismology of Icy Ocean Worlds. *Astrobiology*, *18*(1), 37–53. https://doi.org/10.1089/ast.2016.1612

Vance, S. D., Behounkova, M., Bills, B. G., Byrne, P., Cadek, O., Castillo-Rogez, J., et al. (2021). Distributed Geophysical Exploration of Enceladus and Other Ocean Worlds. *Bulletin of the AAS*, *53*(4), 127. https://doi.org/10.3847/25c2cfeb.a07234f4

Vance, S. D., DellaGiustina, D. N., Hughson, K., Hurford, T., Kedar, S., Marusiak, A. G., et al. (2021). Planetary Seismology: The Solar System's Ocean Worlds. In *Bulletin of the American Astronomical Society* (Vol. 53, p. 129). https://doi.org/10.3847/25c2cfeb.ca102d2f

Wahr, J., Selvans, Z. A., Mullen, M. E., Barr, A. C., Collins, G. C., Selvans, M. M., & Pappalardo, R. T. (2009). Modeling stresses on satellites due to nonsynchronous rotation and orbital eccentricity using gravitational potential theory. *Icarus*, *200*(1), 188–206. https://doi.org/10.1016/j.icarus.2008.11.002

Waite, J. H., Glein, C. R., Perryman, R. S., Teolis, B. D., Magee, B. A., Miller, G., et al. (2017). Cassini finds molecular hydrogen in the Enceladus plume: Evidence for hydrothermal processes. *Science*, *356*(6334), 155–159. https://doi.org/10.1126/science.aai8703

Watters, T. R., Weber, R. C., Collins, G. C., Howley, I. J., Schmerr, N. C., & Johnson, C. L. (2019). Shallow seismic activity and young thrust faults on the Moon. *Nature Geoscience 2019*, 1. https://doi.org/10.1038/s41561-019-0362-2

Weber, R. C., Dimech, J.-L., Phillips, D., Molaro, J., Schmerr, N. C., & Fassett, C. (2018).

Thermal Moonquakes: Implications for Surface Properties. In *Lunar and Planetary Science Conference* (Vol. 49).

West, R. A., Lane, A. L., Hart, H., Simmons, K. E., Hord, C. W., Coffeen, D. L., et al. (1983). Voyager 2 photopolarimeter observations of Titan. *Journal of Geophysical Research: Space Physics*, *88*(A11), 8699–8708. https://doi.org/10.1029/JA088iA11p08699

Winberry, J. P., Anandakrishnan, S., & Alley, R. B. (2009). Seismic observations of transient subglacial water-flow beneath MacAyeal Ice Stream, West Antarctica. *Geophysical Research Letters*, *36*(11), L11502. https://doi.org/10.1029/2009GL037730

Withers, M., Aster, R., Young, C., Beiriger, J., Harris, M., Moore, S., & Trujillo, J. (1998). A Comparison of Select Trigger Algorithms for Automated Global Seismic Phase and Event Detection. *Bulletin of the Seismological Society of America*, *88*(1), 95–106.

Zahnle, K., Schenk, P., Levison, H., & Dones, L. (2003). Cratering rates in the outer Solar System. *Icarus*, *163*(2), 263–289. https://doi.org/10.1016/S0019-1035(03)00048-4

Zimmer, C., Khurana, K. K., & Kivelson, M. G. (2000). Subsurface Oceans on Europa and Callisto: Constraints from Galileo Magnetometer Observations. *Icarus*, *147*(2), 329–347. https://doi.org/10.1006/icar.2000.6456

Zimmer, V. L., & Sitar, N. (2015). Detection and location of rock falls using seismic and infrasound sensors. *Engineering Geology*, *193*, 49–60. https://doi.org/10.1016/j.enggeo.2015.04.007